



A Hybrid Ensemble Adjustment Kalman Filter based High-resolution Data Assimilation System for the Red Sea: Implementation and Evaluation

Item Type	Article
Authors	Toye, Habib;Sanikommu, Siva Reddy;Raboudi, Naila Mohammed Fathi;Hoteit, Ibrahim
Citation	Toye, H., Sanikommu, S., Raboudi, N. F., & Hoteit, I. (2020). A Hybrid Ensemble Adjustment Kalman Filter based High-resolution Data Assimilation System for the Red Sea: Implementation and Evaluation. Quarterly Journal of the Royal Meteorological Society. doi:10.1002/qj.3894
Eprint version	Post-print
DOI	10.1002/qj.3894
Publisher	Wiley
Journal	Quarterly Journal of the Royal Meteorological Society
Rights	Archived with thanks to Quarterly Journal of the Royal Meteorological Society
Download date	2024-03-13 11:06:30
Link to Item	http://hdl.handle.net/10754/664829

**A Hybrid Ensemble Adjustment Kalman Filter based High-resolution Data
Assimilation System for the Red Sea: Implementation and Evaluation**

Habib Toye, Sivareddy Sanikommu, Naila F. Raboudi, and Ibrahim Hoteit*

King Abdullah University of Science and Technology (KAUST),
Thuwal 23955-6900, Saudi Arabia

**Submitted to
Quarterly Journal of the Royal Meteorological Society**

*Corresponding Author: ibrahim.hoteit@kaust.edu.sa

Abstract

A new Hybrid ensemble data assimilation system is implemented with a Massachusetts Institute of Technology general circulation model (MITgcm) of the Red Sea. The system is based on the Data Assimilation Research Testbed (DART) and combines a time-varying ensemble generated by the Ensemble Adjustment Kalman filter (EAKF) with a pre-selected quasi-static (monthly varying) ensemble as used in an Ensemble Optimal Interpolation (EnOI) scheme. The goal is to develop an efficient system that enhances the state estimate and model forecasting skill in the Red Sea with reduced computational load compared to the EAKF. Observations of satellite sea surface temperature (SST), altimeter sea surface height (SSH), and in situ temperature and salinity profiles are assimilated to evaluate the new system. The performance of the Hybrid scheme (here after Hybrid-EAKF) is assessed with respect to the EnOI and the EAKF results. The comparisons are based on the daily averaged forecasts against satellite SST and SSH measurements and independent in situ temperature and salinity profiles. Hybrid-EAKF yields significant improvements in terms of ocean state

This article has been accepted for publication and undergone full peer review but has not been through the copyediting, typesetting, pagination and proofreading process which may lead to differences between this version and the Version of Record. Please cite this article as doi: 10.1002/qj.3894

estimates compared to both EnOI and EAKF, in particular mitigating for dynamical imbalances that affects EnOI. Hybrid-EAKF improves the estimation of SST and SSH root-mean-square-differences by up to 20% compared to EAKF. High-resolution mesoscale eddy features, which dominate the Red Sea circulation, are further better represented in Hybrid-EAKF. Important reduction, by about 75%, in computational cost is also achieved with the Hybrid-EAKF system compared to the EAKF. These significant improvements were obtained with the Hybrid-EAKF after accounting for uncertainties in the atmospheric forcing and internal model physics in the time-varying ensemble.

Keywords: Red Sea; Data Assimilation; MITgcm; DART; Ensemble Adjustment Kalman Filter (EAKF); Ensemble optimal interpolation (EnOI); Hybrid ensemble.

1. Introduction

Ocean forecast models are not perfect owing to uncertainties in their internal physics and inputs, such as initial and boundary conditions, and atmospheric forcing (*Edwards et al., 2015; Hoteit et al., 2018*). In data assimilation, these uncertainties are generally accounted for through the so-called background covariance (BC), which spreads the observations information to all model variables (*Kalnay 2002; Hamill 2006; Bannister 2008*). While the BC varies in time (flow-dependent) in ensemble-based Kalman filters, e.g. Singular Evolutive Interpolated Kalman filter-SEIK (*Pham et al., 1998; Hoteit et al., 2002*), Local Ensemble Transform Kalman Filter-LETKF (*Hunt et al., 2007*) and Ensemble Adjustment Kalman Filter-EAKF (*Anderson, 2001*), other popular assimilation methods such as variational methods and ensemble optimal interpolation (EnOI) use static BCs generated via empirical relations and/or climatological ensembles (*Hoteit et al., 2002; Bonavita et al., 2012; Martin et al., 2015; Stammer et al., 2016*). In these methods, the BC may not account

for the “errors-of-the-day”, which could potentially lead to improved model forecasts (e.g. *Derber and Bouttier*, 1999; *Hoteit et al.*, 2002; *Xie and Zhu*, 2010; *Chen et al.*, 2013; *Waters et al.*, 2017; *Sanikommu et al.*, 2017; *Hoteit et al.*, 2018).

Because of their computational requirements in realistic applications, Ensemble Kalman Filters (EnKFs) are generally implemented with small ensembles (e.g. 20-100 members). EnKFs may also suffer when the sources of model uncertainties are not properly accounted for. These issues lead to severely rank-deficient BCs with noisy (ensemble) correlations and systematically reduced variance (loss of ensemble spread) (see the reviews of *Bannister*, 2017 and *Hoteit et al.*, 2018). This may greatly limit the EnKF’s ability to fit the observations and to produce meaningful ocean state estimates (e.g., *Edwards et al.*, 2015; *Hoteit et al.*, 2018). Various auxiliary techniques have been proposed to mitigate the impact of these limitations. Localization, in which long-range correlations are tapered, is a straightforward and efficient approach to eliminate spurious correlations and increase the BCs rank (*Houtekamer and Mitchell*, 1998; *Hamill et al.*, 2001). Covariance inflation, which inflates the EnKF covariance (forecast or analysis) by some positive factor at each assimilation cycle, is another approach to compensate for the systematic loss in ensemble spread (*Anderson and Anderson*, 2009; *Luo and Hoteit*, 2011). The ad hoc nature of these fixes are, however, known to degrade the dynamical balance of the filter analysis and to increase the forecast errors in sparsely observed regions (e.g. *Anderson* 2009; *Bowler et al.*, 2017; *Sanikommu et al.*, 2017). A Hybrid ensemble scheme, in which BCs are estimated as linear combinations of time-varying ensembles generated by an EnKF with climatological (static) ensembles covariances (e.g. *Hammill and Snyder*, 2000; *Xuguang et al.*, 2007; *Song et al.*, 2010; *Lorenc*, 2015), was proposed to mitigate the aforementioned issues. This increases the EnKF BCs rank and spread, and enforces smoothness in the ocean state estimates. This was found to be particularly beneficial when the filter is implemented with

small ensembles (*Wan et al.*, 2009; *Counillon et al.*, 2009; *Hoteit et al.*, 2010; *Gharamti et al.*, 2014; *Penny et al.*, 2015; *Tsiaras et al.*, 2017).

Various hybrid approaches have been successfully proposed for data assimilation into ocean general circulation models (*Larsen et al.*, 2007; *Counillon et al.*, 2009; *Penny et al.*, 2015; and *Konstantin et al.*, 2018). Here, we follow a similar approach to that of *Xuguang et al.* (2007) and develop a Hybrid-EAKF system for data assimilation into a mesoscale resolving (4km-resolution) Massachusetts Institute of Technology general circulation model (MITgcm; *Marshall et al.*, 1997) of the Red Sea. The system is implemented based on the Data Assimilation Research Testbed (DART; *Anderson et al.* 2001). Our goal is to enhance the EAKF performances, using small flow-dependent ensembles to reduce the computational load. We further derive a practical implementation of the Hybrid-EAKF scheme based on DART.

The Red Sea lies between Africa and the Arabian Peninsula and connects with the Indian Ocean in the south through the narrow strait of Bab-El-Mandeb. It is one of the warmest and saltiest bodies of seawaters in the world (*Belkin et al.*, 2009), yet it hosts a unique ecological system fringed with coral reefs (*Carvalho et al.*, 2019). It features a seasonally-reversing overturning circulation driven by the Indian Monsoon (*Aiki et al.*, 2006; *Yao et al.*, 2014a,b), and important interannual variability in response to major climate phenomenon such as El-Nino-Southern Oscillation (ENSO) and the North Atlantic Oscillation (NAO) (*Raitsos et al.*, 2015; *AbuAlnaja et al.*, 2015; *Yao and Hoteit*, 2018; *Krokos et al.*, 2019). The general circulation of the Red Sea is dominated by series of quasi-stationary mesoscale eddies (*Quadfasel and Baudner*, 1993; *Zhan et al.*, 2014, 2019) and is primarily driven by the overlying atmosphere through wind stress, heat, buoyancy and freshwater fluxes (*Sofianos and Johns*, 2002, 2003; *Yao et al.*, 2014a,b; *Zhan et al.*, 2018). Resolving such features requires an eddy-resolving model. Even after doing so, and unless

the model is constrained with observations using data assimilation, ocean models forecasting skills remain limited in such a complex environment (e.g. *Anderson et al.*, 1996; *Fukumori*, 2001; *Kamachi et al.*, 2002; *Edwards et al.*, 2015; *Martin et al.*, 2015; *Stammer et al.*, 2016; *Hoteit et al.*, 2018; *Moore et al.*, 2019), due to inherent uncertainty in the physical parameterizations, atmospheric forcing, and other model inputs.

Interest in developing data assimilation and forecasting capability for the Red Sea have only grown recently with the initiation of new Saudi national mega developmental projects along the shore of the Red Sea and governmental interest in protecting its resources (*Hoteit et al.*, 2020). *Toye et al.* (2018) successfully implemented an EnOI-based data assimilation system with a 4km-resolution MITgcm of the Red Sea, assimilating observations from satellite sea surface temperature and altimeter sea level anomaly. Despite using monthly-varying climatological ensembles to estimate the static BCs, the ocean forecasts resulting from this EnOI system underlined important dynamical imbalances in the subsurface. In a follow up work, *Sanikommu et al.* (2020) demonstrated that by accounting for uncertainties in the initial conditions, atmospheric forcing, and internal physics, the flow-dependent BCs of the EAKF provide dynamically consistent and improved forecasts throughout the ocean column.

This study proposes a new Hybrid-EAKF combining the EAKF system of *Sanikommu et al.* (2020) and EnOI system of *Toye et al.* (2017). The aim is to further improve the state estimate and model forecasting skill in the Red Sea while alleviating the computational load of the EAKF. The remainder of the paper is organized as follows. Section 2 describes the Hybrid-EAKF. Section 3 outlines the numerical experiments setup, including the description of the ocean model, assimilated observations, and the independent observations used for evaluating the assimilation system. Section 4 discusses the assimilation results in terms of their forecasting skill statistics, and to reproduce basin mesoscale eddy features. It further

analyzes the dynamical balances of the Hybrid-EAKF solutions. The computational load of the Hybrid-EAKF system is discussed in Section 5. Summary and conclusions are provided in Section 6.

2. The Hybrid-EAKF

Data assimilation is the process by which observations are used to update models forecasts in order to compute the best possible estimate of the state of the ocean (*Edwards et al.* 2015; *Hoteit et al.*, 2018). The EAKF is a sequential assimilation scheme that operates as a series of assimilation cycles, each involving a model forecast followed by a filter update (*Anderson*, 2001).

Let $\{\mathbf{x}_i^f\}_{i=1}^{N_d}$ be an ensemble of N_d model forecasts (or priors) and $\bar{\mathbf{x}}^f = \frac{1}{N_d} \sum_{i=1}^{N_d} \mathbf{x}_i^f$ its sample mean. Let also $\mathbf{X}'^f = [\mathbf{x}_1^f - \bar{\mathbf{x}}^f, \mathbf{x}_2^f - \bar{\mathbf{x}}^f, \dots, \mathbf{x}_{N_d}^f - \bar{\mathbf{x}}^f]$ be the ensemble of forecast anomalies and $\mathbf{P}^f = \frac{1}{N_d-1} \mathbf{X}'^f \mathbf{X}'^{fT}$ the forecast error covariance. The EAKF update step can be described as follows (*Anderson* 2001):

$$\bar{\mathbf{x}}^a = \mathbf{P}^a [(\mathbf{P}^f)^{-1} \bar{\mathbf{x}}^f + \mathbf{H}^T \mathbf{R}^{-1} \mathbf{y}^o], \quad (1)$$

$$\mathbf{P}^a = [(\mathbf{P}^f)^{-1} + \mathbf{H}^T \mathbf{R}^{-1} \mathbf{H}]^{-1} \quad (2)$$

where Eqs. (1) and (2) respectively compute the analysis state $\bar{\mathbf{x}}^a$ and its error covariance \mathbf{P}^a from the forecast state $\bar{\mathbf{x}}^f$ and its error covariance \mathbf{P}^f . \mathbf{H} is the observation operator, \mathbf{y}^o the observation, and \mathbf{R} the observational error covariance. An analysis ensemble $\{\mathbf{x}_i^a\}_{i=1}^{N_d}$ is then generated such that its sample mean and covariance exactly match $\bar{\mathbf{x}}^a$ and \mathbf{P}^a . This is achieved by constructing a specific matrix \mathbf{A} such that $\mathbf{P}^a = \mathbf{A} \mathbf{P}^f \mathbf{A}^T$ (see *Anderson*, 2001 for a detailed computation of the matrix \mathbf{A}).

$$\mathbf{x}_i^a = \mathbf{A}(\mathbf{x}_i^f - \bar{\mathbf{x}}^f) + \bar{\mathbf{x}}^a, \quad i = 1, \dots, N_d. \quad (3)$$

The next forecast step can then take place by integrating the $\{\mathbf{x}_i^a\}_{i=1}^{N_d}$ forward with the model to obtain the forecast ensemble at the time of the next available observation. A new update step can then begin.

The Hybrid-EAKF has the same algorithm as EAKF, except for the use of a hybrid forecast error covariance $\mathbf{P}^{f,H}$, expressed as a linear combination of a flow-dependent forecast covariance and a static background covariance (*Hamill and Snyder, 2000*),

$$\mathbf{P}^{f,H} = (1 - \alpha)\mathbf{P}^f + \alpha\mathbf{B}, \quad \text{with } 0 \leq \alpha \leq 1 \quad (4)$$

instead of \mathbf{P}^f in (1)-(2). \mathbf{P}^f is referred to as the flow-dependent covariance, computed from the dynamic propagation of the forecast ensemble \mathbf{X}^f with the EAKF. \mathbf{B} is a static background covariance matrix, which could be estimated from a climatological dataset as in an Ensemble Optimal Interpolation system, or parameterized as in a 3D variational (3DVAR) system (*Song et al., 2010; Lellouche et al., 2013*). The forecast state $\bar{\mathbf{x}}^f$ is then updated as in (1) and (2), using $\mathbf{P}^{f,H}$ instead of \mathbf{P}^f , to obtain the hybrid analysis state $\bar{\mathbf{x}}^{a,H}$ as

$$\mathbf{P}^{a,H} = [(\mathbf{P}^{f,H})^{-1} + \mathbf{H}^T \mathbf{R}^{-1} \mathbf{H}]^{-1} \quad (5)$$

$$\bar{\mathbf{x}}^{a,H} = \mathbf{P}^{a,H} [(\mathbf{P}^{f,H})^{-1} \bar{\mathbf{x}}^f + \mathbf{H}^T \mathbf{R}^{-1} \mathbf{y}^o], \quad (6)$$

The resampling of the analysis members is then performed as in (3), but using $\bar{\mathbf{x}}^{a,H}$ instead of $\bar{\mathbf{x}}^a$.

The Hybrid formulation reduces to EnOI with $\alpha=1$, with the ocean model only used to compute the forecast state from a given analysis. The forecast is then updated with the incoming observations as in (1) and using a static background \mathbf{B} .

2.1. Practical implementation within DART

The Data Assimilation Research Testbed (DART) is a portable software for ensemble data assimilation developed at the National Center of Atmospheric Research (NCAR) (*Anderson et al., 2009*). Exploiting the serial formulation of the Kalman filter update step, DART is configured to integrate and update the ensemble members in parallel using scalable

algorithms of different ensemble filters, including the EAKF (*Anderson and Collins 2007*). DART is further equipped with sophisticated localization and inflation schemes to boost the performance of ensemble data assimilation schemes with small ensembles. We implemented the Hybrid-EAKF in DART by calling separately two EAKF update steps, one to update the forecast anomalies based on the flow-dependent forecast covariance and another to update the forecast mean using the hybrid covariance. Combining the results of the two filters yields a hybrid analysis ensemble with the desired mean and covariance as follows:

- i. The flow-dependent forecast ensemble \mathbf{X}^f is first updated using the EAKF analysis step. This gives an analysis ensemble satisfying Eq. (3), with an analysis mean and covariance respectively given by Eqs. (1) and (2). Rewriting (3) as

$$(\mathbf{x}_i^a - \bar{\mathbf{x}}^a) = \mathbf{A}(\mathbf{x}_i^f - \bar{\mathbf{x}}^f), \quad i = 1, \dots, N_d,$$

suggests that the updated anomalies are simply the updated members from which the analysis mean is removed.

- ii. In order to update the forecast state, a prior ensemble \mathbf{X}^H , based on \mathbf{X}^f and \mathbf{X}^s , is constructed and supplied as input to DART. \mathbf{X}^H is such that by calling a standard EAKF update in DART, the resulting analysis state satisfies Eq. (6) and is expressed as $\mathbf{X}^H = [K_d \mathbf{X}^f, K_s \mathbf{X}^s] + \bar{\mathbf{x}}^f$, with

$$K_d = \sqrt{\frac{(1-\alpha)(N_d+N_s-1)}{N_d-1}} \quad \text{and} \quad K_s = \sqrt{\frac{\alpha(N_d+N_s-1)}{N_s-1}}.$$

\mathbf{X}'^s is a static ensemble perturbation matrix defined as $\mathbf{X}'^s = [\mathbf{x}_1^s - \bar{\mathbf{x}}^s, \mathbf{x}_2^s - \bar{\mathbf{x}}^s, \dots, \mathbf{x}_{N_s}^s - \bar{\mathbf{x}}^s]$ with $\{\mathbf{x}_i^s\}_{i=1}^{N_s}$ an ensemble of N_s members of mean $\bar{\mathbf{x}}^s$ and covariance

$\mathbf{B} = \frac{1}{N_s-1} \mathbf{X}'^s \mathbf{X}'^{sT}$. One can verify that the $(N_d + N_s)$ ensemble \mathbf{X}^H has a mean $\bar{\mathbf{x}}^f$

and a covariance $\mathbf{P}^{f,H}$. The sample covariance of \mathbf{X}^H is indeed given by

$\frac{1}{N_d+N_s-1} \mathbf{X}'^H \mathbf{X}'^{HT}$, where \mathbf{X}'^H is the corresponding perturbation matrix (i.e., $\mathbf{X}'^H =$

$[K_d \mathbf{X}'^f, K_s \mathbf{X}'^s]$). Using the expressions of K_d and K_s , the covariance can be expressed as $\frac{(1-\alpha)}{N_d-1} \mathbf{X}'^f \mathbf{X}'^{fT} + \frac{\alpha}{N_s-1} \mathbf{X}'^s \mathbf{X}'^{sT}$, which is equal to $(1-\alpha)\mathbf{P}^f + \alpha\mathbf{B}$ and thus to $\mathbf{P}^{f,H}$. Finally, since \mathbf{X}^H has a mean $\bar{\mathbf{x}}^f$ and a covariance $\mathbf{P}^{f,H}$, its EAKF update yields an analysis state that matches $\bar{\mathbf{x}}^{a,H}$ given by Eq. (6)

- iii. The hybrid analysis ensemble is then obtained by adding the anomalies resulting from step (i) to the hybrid analysis mean state from step (ii) as

$$\mathbf{x}_i^{a,H} = \bar{\mathbf{x}}^{a,H} + (\mathbf{x}_i^a - \bar{\mathbf{x}}^a), \quad i = 1, \dots, N_d. \quad (7)$$

3. The assimilation system

3.1. The Ocean model - MITgcm

We use a 4km-resolution MITgcm (Marshall *et al.*, 1997) configured for the domain 30°E-50°E and 10°N-30°N covering the whole Red Sea, including the Gulf of Suez, the Gulf of Aqaba, and part of the Gulf of Aden where an open boundary connects it to the Arabian Sea (Figure 1a). The model has 50 vertical layers with 4m resolution in the surface and 300m resolution near the bottom. The bathymetry of the basin is derived from the General Bathymetric Chart of the Ocean (GEBCO, available at http://www.gebco.net/data_and_products/gridded_bathymetry_data). The open boundary conditions (OBCS) for temperature, salinity, and horizontal velocity are prescribed daily from the Global Ocean Reanalysis and Simulation data (GLORYS; Parent *et al.*, 2003) available at 1/12° horizontal grid. A sponge layer of 5 grid boxes with a relaxation period of 1-day is implemented for smooth incorporation of open ocean conditions through the eastern boundary. The model uses a 3rd Order Direct Space Time (DST-3) advection scheme for tracers, harmonic viscosity with a coefficients of 30 m²/s in the horizontal and 7x10⁻⁴ m²/s in the vertical, implicit horizontal diffusion for both temperature and salinity, and the K-Profile Parameterization (KPP) scheme

(Large *et al.*, 1994) for vertical mixing with a background vertical diffusion coefficient of $10^{-5} \text{ m}^2/\text{s}$ for both temperature and salinity.

A long spin up of the model is desirable before utilizing it for forecasting. Here we started the assimilation experiments after a model spin up of 31 year starting from 1979 that was readily available for this study. The European Center for Medium Range Weather Forecast (ECMWF) interim reanalysis (ERA-I) of atmospheric surface fluxes of radiation, momentum, and freshwater were used for the spin up. ERA-I provides 6-hourly fields at 75 km resolution (Dee *et al.*, 2011). For comparison with the assimilation runs (as further discussed in the next Section), we ran the same model configuration for the year 2011 using a 6-hourly 50km x 50km atmospheric forcing, with initial conditions obtained from the spin up run. The atmospheric forcing is the ensemble mean of the 50-member ECMWF atmospheric ensemble as made available through The Observing System Research and Predictability Experiment Interactive Grand Global Ensemble project (THORPEX-TIGGE, Bougeault *et al.*, 2010; Buizza 2014; Swinbank 2016; <https://www.ecmwf.int/en/research/projects/tigge>). We examined the free-run outputs forced with the atmospheric ensemble mean and with different ensemble members. The differences between these experiments were negligible (results not shown for brevity). The MITgcm simulations forced with the atmospheric ensemble mean show similar high-resolution features compared to those resulting from simulations forced with an individual member. Here after, we refer to the free-run (without assimilation) forced with the atmospheric ensemble mean as *Fexp*. The Red Sea MITgcm outputs have been extensively validated in several studies (e.g. Yao *et al.*, 2014a, b; Dreano *et al.*, 2016; Toye *et al.*, 2017; Gittings *et al.*, 2018; Zhan *et al.*, 2018, 2019).

3.2. Assimilation experiments

All the assimilation experiments were conducted based on the routines provided in DART. Except for the differences discussed in the next two paragraphs, the experiments were all

performed using the configuration described in *Sanikommu et al.* (2020), with the same settings in terms of assimilated observations, assimilation cycle of 3 days, localization (only in the horizontal direction) using a radius of 300 km, and no-inflation during assimilation. The system assimilates the *Reynolds et al.*, (2007) level-4 daily SST data available on a $0.25^\circ \times 0.25^\circ$ grid (which was prepared by blending in situ observations with data from the advanced very high resolution radiometer infrared satellite; Figure 1b), along-track satellite level-3 merged altimeter filtered sea level anomalies (SLA; corrected for dynamic atmospheric, ocean tide, and long wavelength errors; Figure 1c) from the Copernicus Marine Environment Monitoring Service (CMEMS; *Mertz et al.*, 2017), and in situ temperature and salinity (Figure 1d) profiles from the EN4.2.1 dataset (*Good et al.*, 2013). For direct comparison with the model SSH during assimilation, SLA is added to a mean sea surface height (MSSH) estimated from a long model run between 2002 and 2016 with the best available (5km) resolution atmospheric forcing that has been dynamically downscaled from the 75km ECMWF atmospheric reanalysis using an assimilative Weather Research and Forecast (WRF) model (*Viswanadhapalli et al.*, 2017). One may also consider estimating the MSSH by assimilating in situ temperature and salinity profiles over a long period (*Balmaseda et al.*, 2013 and *Zuo et al.*, 2019). Since our assimilation experiments are only conducted over year 2011, the MSSH simulated by the high resolution atmospheric forcing is the best available for testing the different assimilation schemes.

The observational error covariance matrix is diagonal with temporally-static and spatially-homogeneous observational error variance values of $(0.04 \text{ m})^2$, $(0.5^\circ\text{C})^2$ and $(0.3\text{psu})^2$ for the satellite along-track SSH, the in situ T and S, respectively, and spatio-temporal error variances for the satellite blended level-4 SST, varying between $(0.1^\circ\text{C})^2$ and $(0.6^\circ\text{C})^2$. These relatively large error variances for T and S, which are chosen in accordance with the suggested ranges of in situ observational errors in earlier assimilation studies (e.g.,

Richman et al., 2005; *Forget and Wunsch*, 2007; *Oke and Sakov*, 2008; *Karspeck*, 2016), are intended to account for the representational errors due to unresolved scales and processes in the model (*Sanikommu et al.* 2019). The SLA observational error of $(0.04 \text{ m})^2$, which is slightly larger than the suggested altimeter accuracy (AVISO 2015), is selected based on a sensitivity experiment with various values of error variances, $(0.04 \text{ m})^2$, $(0.07 \text{ m})^2$, and $(0.1 \text{ m})^2$ (results not shown here; discussed in *Sanikommu et al.*, 2020). Since our 4km-MITgcm can resolve the scales of the 25km x 25km assimilated SST data, only measurements errors of SST data are considered. The specified observational error variances for SST vary in accordance with the analysis errors specified in the level-4 gridded SST product of *Reynolds et al.* (2007).

Table 1 and 2 summarize the configurations of the conducted experiments. Three different categories of assimilation experiments are analyzed: *EnOIexp*, *EAKFexp*, and *HyBDexp*. *EnOIexp* employs the same model configuration as *Fexp* and assimilates observations with EnOI, starting from the 1st January, 2011 ocean state obtained from *Fexp*. *EnOIexp* is implemented with a monthly-varying 250-member ensembles, generated as in *Toye et al.* (2017) using the last 15 year model hindcasts of the spin up run. *EAKFexp* assimilates the observations using EAKF, with a flow-dependent background ensemble of 50 members. The initial ensemble in *EAKFexp* is generated by randomly selecting 50 different states corresponding to January's hindcasts of *Fexp* and then re-centering the ensemble mean to the 1st January, 2011 state of *Fexp*. The MITgcm forecasts of the 50 members were forced with the ECMWF ensemble atmospheric forcing. Different model physics were also used for integrating each member, selected from a time-varying ensemble of model physics (hereafter model physics dictionary, MPD). The MPD encompasses different choices of vertical and horizontal mixing schemes, and viscosity and diffusivity coefficients. These include five types of horizontal diffusion, three schemes of horizontal viscosity, and four schemes of

vertical mixing as listed in Table 3. More details about the generation of the MPD and of the physical perturbation impact on the assimilation results can be found in *Sanikommu et al.* (2020). *HyBDexp* is implemented by combining the 250-member quasi-static ensemble (used in *EnOIexp*) with a 50-member dynamic ensemble with a weighing factor (α) of 0.05, selected after examining the sensitivity of the Hybrid system to the choice of α . More details about the results of these sensitivity experiments are presented in Section S1 of the Supplementary Materials. *HyBDexp* uses the same initial and atmospheric forcing ensembles, and perturbed internal physics as those of *EAKFexp*. *EnOIexp* was also tested with 300 members and the results were very similar to those of the 250-member case.

Figure 2 displays the ensemble spread of (a) SST and (b) SSH from *HyBDexp* and *EAKFexp*. It also shows the spread of the quasi-static ensemble before and after scaling its ensemble covariance by a factor of 0.05 (the weighing factor of *HyBDexp* α). The ensemble SSH spread varies between 2-4cm in *HyBDexp* and *EAKFexp*. The spread of the EnOI-ensemble is significantly larger, but becomes closer to those of *HyBDexp* and *EAKFexp* after the scaling of the quasi-static ensemble covariance. The assimilation results of the experiments using the quasi-static ensemble (here after *EnOIInoSCLexp*) and those using the scaling of the quasi-static ensemble covariance (*EnOIexp*) in the EnOI system suggests that this scaling has no significant impact on SST (Figures 3a). It however shows noticeable impact on SSH (Figure 3b), with the *EnOIexp* exhibiting lower RMSDs compared to *EnOIInoSCLexp*. The most pronounced differences between the results of *EnOIInoSCLexp* and *EnOIexp* are found in the data-sparse subsurface layers and for under-sampled ocean variables. *EnOIInoSCLexp* simulates spurious fresh water anomalies in the surface (Figures 4c and 4d) and in the subsurface layers (Figure not shown). Such spurious features are likely due to dynamical imbalances, which can be assessed through vertical velocities (e.g., *Sanikommu et al.*, 2020). The maximum vertical speed in the water column, $|W(z)|_{max}$, a proxy for 2D

visualization of the abnormal vertical velocities in the ocean column, is suspiciously large in *EnInoSCLexp* compared to *Fexp* (Figure 6a and 6b), suggesting important dynamical imbalances in the EnOI before scaling the quasi-static ensemble covariance. *EnOIexp* results in better estimates of the ocean state (Figures 3a, 3b, and 4d) with lesser dynamical imbalances (Figure 6c). We therefore evaluate the results of *HyBDexp* against those of *EnOIexp*, the best possible EnOI configuration.

3.3. Validation data

The daily averaged forecasts from the different experiments are analyzed to assess the performances of the different assimilation configurations. Subsurface estimates are evaluated against CTD observations of temperature and salinity profiles collected in the Red Sea between 15th September and 8th October, 2011 (indicated in Figure 4a). This dataset includes 206 profiles collected by a joint Woods Hole Oceanography Institute (WHOI) and King Abdullah University of Science and Technology (KAUST) cruise along the eastern Red Sea, with a horizontal spacing of 10km (*Zhai et al.*, 2015; hereafter WHOI/KAUST summer cruise). Root-Mean-Square-Differences (RMSD) of the daily averaged forecasts of SST and SSH are computed with respect to merged satellite level-3 observations of Group for High Resolution Sea Surface Temperature (GHRSSST; *EUMETSAT*, 2008) and merged along track level-3 altimeter observations of SSH from CMEMS (*Mertz et al.*, 2017), respectively. In order to evaluate the relative performance of the assimilation experiments against the interpolated products, we employed level-4 products of SST and SSH. The interpolated SST product is a high-resolution daily averaged level-4 SST product from the OSTIA (Operational Sea Surface Temperature and Sea Ice Analysis; *Stark et al.*, 2007; *Donlon et al.*, 2012). OSTIA is generated on a 0.054° (~ 6 km) grid by combining SST data from various satellites and in situ observations using an Optimal Interpolation (OI) system. The interpolated SSH product is the multi-mission altimeter merged satellite level-4 gridded

Absolute Dynamic Topography (ADT) provided by CMEMS (here after CMEMS-L4; *Mertz et al.*, 2017). The ADT is available daily at $0.25^\circ \times 0.25^\circ$ resolution. The maximum formal ADT mapping error (provided along with the CMEMS-L4 ADT product) during the analysis period 1st January-31st December, 2011 is estimated between 1.8 cm - 4 cm in the southern RS and reaches up to 7cm in the northern Red Sea. The CMEMS-L4 ADT is adjusted by replacing its 15-year average with the model mean SSH for direct comparison with the model SSH, similar to the treatment of the assimilated along-track SLA data (see Section 3.2). WHOI/KAUST observations are not assimilated and are therefore used as an independent observations for validation. The assimilated SST and SSH observations were used in the generation of the interpolated level-4 products of OSTIA and CMEMS, and as such these datasets cannot be considered to be fully independent from our assimilated fields.

4. Evaluation of the Hybrid system

This section evaluates the outputs of *HyBDexp* compared to those of *EnOIexp* and *EAKFexp*. We first establish the merits and demerits of *EnOIexp* and *EAKFexp*, and then investigate how well these are addressed in *HyBDexp*. Figure 3 displays the temporal evolution of (a) SST and (b) SSH RMSDs for entire model domain. RMSDs of SST and SSH are comparatively large and exhibit seasonal dependencies in *Fexp*, with relatively large SST (SSH) RMSDs during summer (winter). The increased SST RMSDs during summer are due to biases in the summer atmospheric fields in the southern Red Sea associated with dust (*Viswanadhapalli et al.*, 2017). The increased SSH RMSDs during winter can be related to biases in the surface net heat flux associated with increased atmospheric convective activity (*Viswanadhapalli et al.*, 2017), which affects strong eddies in the northern Red sea (*Yao et al.*, 2014b; *Zhan et al.*, 2014; *Zhan et al.*, 2018). Assimilation using EnOI or EAKF significantly improves the RMSDs for both SST and SSH, with consistently smaller RMSDs throughout the year. The RMSDs of SST and SSH in these assimilation experiments are even

lower than the interpolated products. The SST and SSH RMSDs differences between *EnOIexp* and *EAKFexp* are relatively small, with *EnOIexp* yielding slightly better results. For instance, while the SST RMSD (SSH RMSD) corresponding to the whole domain and full year-2011 is 0.68 °C (4.9 cm) in *EnOIexp*, it is 0.71 °C (5.1 cm) in *EAKFexp*. Examining region wise statistics of SST and SSH suggests that the differences between these two experiments are noticeable only in the Gulf of Aden (figures/table not shown), with the EnOI yielding better results compared to EAKF. One may expect the results of *EAKFexp* to improve if uncertainties in the ocean boundary conditions were accounted for (through appropriate perturbations), as this should enhance its the ensemble spread in the Gulf of Aden.

To provide more insight into the results for under-sampled regions and ocean variables, we examined the assimilation solution for sea surface salinity (SSS) and subsurface temperature and salinity using independent observations from the WHOI/KAUST. Figure 4 displays spatial maps of SSS from the different experiments overlaid with independent observations from WHOI/KAUST summer cruise. Interestingly, the SSS results are very different from the SST and SSH results, with *EAKFexp* performing significantly better than *EnOIexp*. For instance, the observations indicate a north-south gradient with fresh-water in the southern Red Sea and saline-water in the northern RS (Figure 4a). Such a prominent north-south salinity gradient is not well reproduced in *EnOIexp* (Figure 4d). *EnOIexp* simulates a spurious fresh water pool in the central Red Sea influenced by the advection of anomalous fresh waters from the southern Red Sea, where the SSS differences between observations and *EnOIexp* reach 2 psu. These biases are even larger than that in *Fexp* (Figure 4b). The SSS from *EAKFexp*, on the other hand, agrees much better with the observations (compare Figure 4e with 4b and 4c), with the model-data differences being less than 1 psu, and improved north-south spatial gradients of SSS. Figure 5 plots the estimated temperature

and salinity structures corresponding to the WHOI/KAUST summer cruise observations locations. *EnOIexp* exhibits a salinity bias of 0.5 psu in the subsurface layers throughout the domain (Figure 5d), and simulates spurious pockets of high salinity waters in the subsurface layers (180-300m) between 22°-24°N (absolute fields from the assimilation experiments are not shown in the Figure). $|W(z)|_{max}$ is suspiciously large (compared to *Fexp*; Figures 6c with 6a) in *EnOIexp* almost throughout the Red Sea starting from the middle of the year. As argued in *Sanikommu et al.* (2020), such a large $|W(z)|_{max}$ results from spurious vertical correlations in the quasi-static ensemble of the *EnOIexp*. *EAKFexp* does not show such sporadic behavior. It further improves the subsurface temperature and salinity biases particularly to the north of 20°N. However, as already reported in *Sanikommu et al.* (2020), *EAKFexp* misses high-resolution spatial features such as the deepening of the 23°C isotherm around 26°N (compare Figure 5e with 5a), the intrusion of a fresh and cold Gulf-of-Aden water mass around 60m (which manifest itself as large overestimation of subsurface temperature and salinity south of 20°N; Figure 5e-f). *EnOIexp* reproduces these features, but with significant discrepancies in the location of the deeper 23°C isotherm and in the magnitudes of the temperature/salinity of the GoA water mass appearing at the intermediate layers. This is likely related to spurious propagations of surface observations information (*Sanikommu et al.*, 2017, 2019) due to the misrepresentation of the “errors-of-the-day” by the quasi-static ensemble of the EnOI. Such spurious corrections were shown to disrupt the model dynamical balances (*Hoteit et al.*, 2002; *Anderson* 2009; *Penny et al.*, 2013; *Lee et al.*, 2017; *Bowler et al.*, 2017; *Sanikommu et al.*, 2020), particularly in the data-sparse subsurface layers (e.g. temperature and salinity) and for under-sampled ocean variables (e.g. SSS).

HyBDexp significantly improves the Red Sea state estimates and also better preserves the dynamical consistency (as can be inferred from reasonable $|W(z)|_{max}$ in Figure 6e). Note that the larger SST and SSH improvements achieved in *EnOIexp* and *EAKFexp* are not

compromised in *HyBDexp*. *HyBDexp* indeed does even better than *EnOIexp*, in terms of SSH RMSDs (Figure 3b). The SST and SSH RMSDs are improved by up to 20% in *HyBDexp* compared to *EAKFexp*, reaching 0.2°C and 1cm in terms of differences in SST and SSH RMSDs, respectively. SSS (an under-sampled variable) in *HyBDexp*, which was not well simulated by *EnOIexp* and better represented in *EAKFexp*, is closer to the observations in the southern Red Sea with *HyBDexp*. The SSS is even better estimated by *HyBDexp* compared to *EAKFexp* in this region (compare Figure 4f with 4d and 4e). The differences between *HyBDexp* and *EAKFexp* SSS are not very significant over the rest of the domain. Subsurface temperature and salinity are better reproduced by *HyBDexp* (Figure 5g-h) compared to *EnOIexp* (Figure 5c-d). In addition, *HyBDexp* does better than *EAKFexp* (Figure 5e) in capturing the subsurface temperature structure, particularly the deepening of the 23°C isotherm in the northern latitudes, which was completely missed in *EAKFexp*. The large subsurface salinity biases introduced by the quasi-static ensemble are however not fully mitigated in *HyBDexp* (Figure 5h).

4.1. Impact of Hybrid on Mesoscale Eddy Features.

To demonstrate the merits of the *HyBDexp* system in reproducing the Red Sea mesoscale eddy features, spatial maps of SSH snapshots are shown in Figure 7, where clear differences can be seen between *HyBDexp* and *EAKFexp* in the northern Red Sea, central Red Sea, and Gulf of Aden (GoA). Figure 7 displays along-track SSH observations on 6th November, 2011 (top), 15th July, 2011 (middle), and 30th September, 2011 (bottom) overlaid on the corresponding daily averaged spatial maps from *CMEMS-L4* (left), *EAKFexp* (middle) and *HyBDexp* (right). The 6th November, 2011 corresponds to a period of an anomalous cyclonic eddy (CE) in the northern Red Sea (Figure 7a) (*Papadopoulos et al.*, 2015). It is largely modulated by the local net heat flux and remote sea level perturbations from the southern Red Sea (*Zhan et al.*, 2018). Around 15th July, 2011, the central Red Sea hosted an anti-cyclonic

eddy (ACE) around 21°N (Figure 7b). Such an eddy, whose presence may have been tied to coastline and topographic variations (e.g. *Quadfasel and Baudner*, 1993), appears every June and lasts until July (e.g. *Raitsos et al.*, 2013). Around 30th September, 2011 the Gulf-of-Aden experienced a series of eddies (Figure 7c), which results from instabilities in the adjacent Somali current and in the nearby large eddies, such as the Great whirl and Socorta eddy (*Al Saafni et al.*, 2007; *Yao and Hoteit*, 2014).

Comparing the assimilation estimates with SSH observations (for both along-track SSH and interpolated product *CMEMS-L4*) suggests that the intensity and the size of the eddies are underestimated in *EAKFexp* (Figure 7d-f). *EAKFexp*, for instance, completely misses the ACE in the central Red Sea. *HyBDexp* significantly improves the eddy features in terms of their intensity and also size, irrespective of the region (Figure 7g-i). For instance, the missed ACE in *EAKFexp* (Figure 7e) is reproduced reasonably well by *HyBDexp* (Figure 7h), albeit slightly shifted. The intensities of the series of alternating eddies in the GoA, and the anomalous CE in the northern Red Sea, are also better represented in *HyBDexp* (Figure 7i) than in *EAKFexp* (Figure 7f). In fact, *HyBDexp* is a closer match to the observations than *CMEMS-L4* (Figure 7a-c) in terms of eddies intensities.

4.2. Importance of accounting for background errors due to uncertainties in internal model physics and atmospheric forcing in the Hybrid system

Sanikommu et al. (2020) demonstrated the importance of accounting for background errors due to uncertainties in the internal ocean model physics and atmospheric forcing in the EAKF. To examine the significance of these in the Hybrid system, we have conducted two more *HyBDexp* experiments, *HyBDmAPexp* and *HyBDmPexp*. *HyBDmAPexp* and *HyBDmPexp* are the same as *HyBDexp* except that *HyBDmAPexp* uses the default internal model physics and is forced by the ensemble mean ECMWF atmospheric fields, and *HyBDmPexp* uses the default internal model physics and is forced by the ensemble ECMWF

fields. Figure 6f and 6g display $|W(z)|_{max}$ along the Red Sea axis from *HyBDmAPexp* and *HyBDmPexp*, respectively. Compared to *HyBDexp*, the spread of the large $|W(z)|_{max}$ becomes wider in *HyBDmPexp*, and even wider in *HyBDmAPexp*, suggesting degraded dynamical balances. This is even manifested in SSS, and subsurface temperature and salinity. For instance, as can be seen from Figures 4g and 4h, the north-south SSS gradient is not well represented in *HyBDmAPexp* and *HyBDmPexp* compared to *HyBDexp*. They also show anomalous fresh waters in the southern parts of the Red Sea. The subsurface temperature (Figures 5i and 5k) and salinity (Figure 5j and 5l) also become noisy, and show spurious features and increased biases. These results clearly emphasize the importance of accounting for uncertainties in the atmospheric forcing and internal model physics in the Hybrid system.

5. Impact of Hybrid in terms of computational gain

This section focuses on assessing *HyBDexp* in terms of computational efficiency, an important aspect of this study. This is achieved by first assessing the sensitivity of EAKF ocean state estimates to gradually increased ensemble size.

We first present results from four different EAKF experiments: the standard 50-member *EAKFexp*, *EAKF100exp*, *EAKF250exp*, and *EAKF500exp*. The last three experiments are similar to *EAKFexp* but use 100, 250, and 500 ensemble members, respectively. Table 2 outlines the configurations of these experiments. The initial ensembles of these experiments are generated as in *EAKFexp*, and the atmospheric forcing is sampled, assuming a normal distribution, using the ensemble mean and spread of the original 50-member ensemble atmospheric forcing of *EAKFexp*. Examining the assimilation results of these experiments suggests little differences in terms of SST and SSH (Figures not shown), which is expected owing to the homogeneous observations coverage of these datasets. No clear differences in the results are found for the sparsely observed temperature variable either. More pronounced differences are obtained however with salinity, the most under-

sampled variable, both at surface and subsurface. Increasing the size of the ensemble from 50 to 100 reduces salinity biases in the intermediate layers (Figure 8b). Noticeable improvements in the salinity are also achieved in the whole water column when increasing the ensemble size from 100 to 250. Comparing the spatial maps of SSS of these EAKF experiments (Figures 9a-d) with the in situ observations suggest that errors in SSS seem to reach a plateau after using 250 ensemble members. Further increasing the size of the ensemble from 250 to 500 resulted in negligible improvements, suggesting that 250 members are enough to describe the statistics of the filtering errors given the considered uncertainties (from ECMWF ensemble forcing and perturbed physical parameterizations) in the system. The SSS and subsurface salinity in *EAKF250exp* (Figures 8c and 9c) are clearly comparable or slightly better than those of *HyBDexp* (Figure 5h and 9e). However, overall, *EAKF250exp* results are still not as good as *HyBDexp*, with substantial differences between the two in terms of SST and SSH, and subsurface temperatures (Figures not shown, as SST and SSH RMSDs and subsurface temperatures in *EAKF250exp* are very similar to those of *EAKFexp*, and Figures 3 and 5 have already outlined the better performances of *HyBDexp*).

To assess the sensitivity of the Hybrid ensemble system to the flow-dependent and static ensembles sizes, we examined the outputs of *HyBDexp* by gradually decreasing the number of flow-dependent members from 50 to 10 while maintaining the ensemble size at 300 members. As summarized in Table 2, these experiments, *HyBD10exp*, *HyBD20exp*, *HyBD30exp*, are the same as the *HyBDexp* (50 dynamical + 250 Static) experiment, but use less flow-dependent members and more static members: 10+290, 20+280, 30+270, respectively. Comparing the results of these experiments (figures not shown) suggests insignificant changes in SST, SSH and in the subsurface temperature and salinity. Though not substantial, the results differ mainly for SSS. Decreasing the size of the dynamic-ensemble from 50 to 30 slightly degrades SSS (compare Figures 9f and 9e), particularly in the southern

parts of the Red Sea. We also see slight degradations in SSS when the dynamic-ensemble size is decreased from 30 to 20 (Figure 9g) and from 20 to 10 (Figure 9h). Overall, all *HyBDexp* experiments, including *HyBD10exp*, are at least as good as *EAKF250exp*.

We finally discuss the computational savings achieved by the *HyBDexp* system, comparing the CPU-hours of *EAKF250exp*, *HyBD10exp*, and *HyBDexp* on our high performance supercomputer facility SHAHEEN-II (<https://hpc.kaust.edu.sa>). Table 4 outlines the break-up of computational load of these experiments for an arbitrary assimilation cycle. The 4km-MITgcm of the Red Sea (array size = 500 x 500 x 50) running with 200s integration time steps on 3 nodes (each node contains 32 cores with 128 GB flash memory) consumes 4.5 core hours for a 3 day integration, the length of the assimilation cycle. The update step with DART consumed 40 core hours for 250-member ensemble when implemented on 20 nodes. *EAKF250exp* consumed 1180 core-hours to complete one assimilation cycle (update+forecast). *HyBDexp* (*HyBD10exp*) calls the DART update step twice, consuming $7+40=47$ ($3+40=43$) core-hours. The total computational cost of *HyBDexp* (*HyBD10*), which integrates 50 (10) MITgcms, is 275 (89) core-hours. This means that the Hybrid systems (here *HyBDexp* and *HyBD10exp*) led to a 76-92% CPU-hours saving with respect to the EAKF-based system (*EAKF250exp*).

6. Summary and conclusions

A new Hybrid data assimilation system was developed for the Red Sea using a 4km-MITgcm and DART. It combines static, but seasonally varying, ensemble members and EAKF-flow-dependent members. The dynamical EAKF members were forecasted with MITgcm forced with atmospheric forcing ensembles and perturbed internal physics. EnOI and EAKF have their own merits and the new Hybrid-EAKF system was able to further improve their performance and helped mitigating their limitations. EnOI was shown to enhance the SST and SSH estimates compared to the EAKF, but degraded the ocean estimates in the under-

sampled regions and variables, such as subsurface temperature, salinity and SSS. It further disturbed the dynamical balances of the ocean state. EAKF better preserved the dynamical balances and better represented the under-sampled variables. It was however less efficient at capturing some of the high resolution features, which are important components of the Red Sea circulation. By complementing the flow-dependent ensemble with static members, the Hybrid-EAKF system was able to capture most of the high resolution mesoscale eddy features, and yielded noticeable improvements in SSH, subsurface temperature, and SSS compared to both EnOI and EAKF. In the deeper layers, EAKF salinity estimates remained relatively better than the Hybrid estimates, when evaluated against the few available subsurface observations. Hybrid-EAKF further outperformed EAKF with 250 members. Reducing the number of dynamical members from 50 to 10 did not significantly affect the Hybrid results, but led to drastic (more than 75% in our setup) computational savings compared to the EAKF systems.

The significant improvements, in terms of both quality of ocean state estimates and computational cost, offered by the Hybrid-EAKF system is a motivation for both ocean data assimilation and operational communities developing ensemble data assimilation systems in the Red Sea and other regional seas. The fact that the Hybrid-EAKF outperforms the best performing EAKF system (that saturated at 250 members), even when accounting for uncertainties in the atmospheric forcing and internal physics, suggests that the EAKF system is still missing some sources of uncertainties. Uncertainties in the open boundary conditions or bathymetry may be part of these imperfections, and will be considered in our future work.

Acknowledgements

This work was funded by the Office of Sponsored Research (OSR) at KAUST under the Virtual Red Sea Initiative (Grant #REP/1/3268-01-01). All the model experiments were run on the KAUST supercomputing facility, SHAHEEN-II. The support of KAUST

supercomputing team is highly acknowledged. The ensemble ocean data assimilation system is implemented with the ROCOTO workflow (<https://github.com/christopherwharrop/rocoto/wiki/Documentation>). Authors hereby declare no conflict of interest. In situ temperature and salinity of EN4.2.1 dataset is downloaded from <https://www.metoffice.gov.uk/hadobs/en4/download-en4-2-1.html>

References

- Abualnaja, Y., V.P. Papadopoulos, S.A. Josey, I. Hoteit, H. Kontoyiannis, and D.E. Raitsos (2015). Impacts of climate modes on air-sea heat exchange in the Red Sea. *Journal of climate*, 28, 7, 2665-2681, DOI:10.1175/JCLI-D-14-00379.1.
- Aiki, H., K. Takahashi, and T. Yamagata (2006). The Red sea outflow regulated by the Indian Monsoon. *Continental Shelf Research*, 26, 12-13, 1448-1468, DOI:10.1016/j.csr.2006. 02.017.
- Anderson D.L.T., J. Sheinbaum, and K. Haines (1996). Data assimilation in ocean models. *Rep. Prog. Phys.*, 59, 1209-1266, DOI:10.1088/0034-4885/59/10/001.
- Anderson, J.L. (2001) An ensemble adjustment Kalman filter for data assimilation. *Mon Weather Rev* 129:2884–2903, DOI: 10.1175/1520-0493(2001)129<2884:AEAKFF>2.0.CO;2.
- Anderson, J. L., and S. L. Anderson (1999). A Monte Carlo implementation of the nonlinear filtering problem to produce ensemble assimilations and forecasts. *Mon. Wea. Rev.*, 127, 2741–2758, DOI:10.1175/1520-0493(1999)127<2741:AMCIOT>2.0. CO;2
- Anderson, J.L., and N. Collins (2007). Scalable Implementations of Ensemble Filter Algorithms for Data Assimilation. *J. Atmos. Oceanic Technol.*, **24**, 1452–1463, DOI:10.1175/JTECH2049.1.
- Balmaseda, M.A., K. Mogensen, and A.T. Weaver (2013). Evaluation of the ECMWF ocean reanalysis system ORAS4. *Q. J. R. Meteorol. Soc.*, 139: 1132-1161, DOI:10.1002/qj.2063.
- Bannister, R.N. (2008). A review of forecast error covariance statistics in atmospheric variational data assimilation. II: Modelling the forecast-error covariance statistics. *Q. J. R. Meteorol. Soc.*, 134, 1971-1996, DOI:10.1002/qj.339.

- Bannister, R. N. (2017). A review of operational methods of variational and ensemble-variational data assimilation. *Q. J. R. Meteorol. Soc.*, 143, 607-633, DOI:10.1002/qj.2982.
- Belkin, I.M., P.C. Cornillon, and K. Sherman (2009). Fronts in large marine ecosystems. *Prog Oceanogr.* 81:223–236, DOI:10.1016/j.pocean.2009.04.015.
- Bougeault, P., Z. Toth, C. Bishop, B. Brown, D. Burridge, D. Chen, E. Ebert, M. Fuentes, T. Hamill, K. Mylne, J. Nicolau, T. Paccagnella, Y.-Y. Park, D. Parsons, B. Raoult, D. Schuster, P. Silva Dias, R. Swinbank, Y. Takeuchi, W. Tennant, L. Wilson and S. Worley (2010). The THORPEX Interactive Grand Global Ensemble (TIGGE). *Bull. Amer. Met. Soc.*, 91, 1059–1072, DOI:10.1175/2010BAMS2853.1.
- Bonavita, M., L. Isaksen, and E. Holm (2012). On the use of EDA background error variances in the ECMWF 4D-Var. *Q. J. R. Meteor. Soc.*, 138, 1540-1550, DOI: 10.1002/qj.1899.
- Buizza, R. (2014). The TIGGE medium-range, global ensembles. *Tech. Rep.. ECMWF*, Shinfield Park, Reading RG2-9AX, UK.
- Carvalho, S., E. Aylaga, R. Villalobos, Y. Kattan, M. Berumen, and J.K. Pearman (2019). Beyond the visual: using metabarcoding to characterize the hidden reef cryptobiome, *Pro. of the Royal Soc.B Biological Sciences*, 286, 1896, DOI:10.1098/rspb.2018.2697.
- Chen, Y., S. R. H. Rizvi, X.-Y. Huang, J. Min, and X. Zhang (2013). Balance characteristics of multivariate background error covariances and their impact on analyses and forecasts in tropical and Arctic regions. *Meteorol Atmos Phys.*, 121, 79–98, DOI: 10.1007/s00703-013-0251-y
- Counillon, F., P. Sakov, and L. Bertino (2009). Application of a hybrid EnKF-OI to ocean forecasting. *Ocean Sci. Discuss.*, 6, 653-688, DOI:10.5194/os-5-389-2009.

- Cox, M.D. (1987). An isopycnal diffusion in a z-coordinate ocean model. *Ocean modelling*, 74, 1-5.
- Danabasoglu, G. and J.C. Mc Williams (1995). Sensitivity of the Global Ocean Circulation to Parameterizations of Mesoscale Tracer Transports. *J. Climate*, 8, 2967–2987, DOI:10.1175/1520-0442(1995)008<2967:SOTGOC>2.0.CO;2
- Dee, D.P., S.M. Uppala, A.J. Simmons, P. Berrisford, P. Poli, S. Kobayashi, U. Andrae, M. A. Balmaseda, G. Balsamo, P. Bauer, P. Bechtold, A. C. M. Beljaars, L. van de Berg, J. Bidlot, N. Bormann, C. Delsol, R. Dragani, M. Fuentes, A. J. Geer, L. Haimberger, S. B. Healy, H. Hersbach, E. V. Hólm, L. Isaksen, P. Kållberg, M. Köhler, M. Matricardi, A. P. McNally, B. M. Monge-Sanz, J. J. Morcrette, B. K. Park, C. Peubey, P. de Rosnay, C. Tavalato, J. N. Thépaut, and F. Vitart (2011). The ERA-Interim reanalysis: configuration and performance of the data assimilation system. *Q. J. R. Meteorol. Soc.* 137(656), 553–597, DOI: 10.1002/qj.828.
- Derber J.C., and F. Bouttier (1999). A reformulation of the background error covariance in the ECMWF global data assimilation system. *Tellus A*, 51, 195–221, DOI:10.1034/j.1600-0870.1999.t01-2-00003.x.
- Donlon C.J., M. Martin, J. Stark, J. Roberts-Jones, E. Fiedler, W. Wimmer (2012). The Operational Sea Surface Temperature and Sea Ice Analysis (OSTIA) system. *Remote Sensing of Environment*, 116, 140-158, DOI:10.1016/j.rse.2010.10.017.
- Dreano, D., D.E. Raitsos, J. Gittings, G. Krokos, and I. Hoteit (2016). The Gulf of Aden intermediate water intrusion regulates the southern Red Sea summer phytoplankton blooms. *Plos One*, 11, 12, DOI: 10.1371/journal.pone.0168440.

- Edwards, C.A., A.M. Moore, I. Hoteit, and B.D. Cornuelle (2015). Regional ocean data assimilation. *Annu. Rev. Mar. Sci.*, 7, 21–42, DOI:10.1146/annurev-marine-010814-015821.
- Fukumori, I. (2001). Data assimilation by models. *Int. Geophys.*, 69, 237–265, DOI: 10.1016/S0074-6142(01)80150-9.
- Gaspar, P., Y. Grégoris, and J.M. Lefevre (1990), A simple eddy kinetic energy model for simulations of the oceanic vertical mixing: Tests at station Papa and long-term upper ocean study site, *J. Geophys. Res.*, 95(C9), 16179– 16193, DOI:10.1029/JC095iC09p16179.
- Gent, P.R. and J.C. McWilliams (1990). Isopycnal Mixing in Ocean Circulation Models. *J. Phys. Oceanogr.*, **20**, 150–155, DOI:10.1175/1520-0485(1990)020<0150: IMIOCM>2.0.CO;2.
- Gent, P.R., J. Willebrand, T.J. McDougall, and J.C. McWilliams (1995). Parameterizing Eddy-Induced Tracer Transports in Ocean Circulation Models. *J. Phys. Oceanogr.*, 25,463–474, DOI:10.1175/1520-0485(1995)025<0463:PEITTI>2.0.CO;2.
- Gittings, J.A., E. Raitos, G. Krokos, and I. Hoteit (2018). Impacts of warming on phytoplankton abundance and phenology in a typical tropical marine ecosystem. *Scientific Reports*, 8(1), 1-12, DOI:10.1038/s41598-018-20560-5.
- Good, S.A., M.J. Martin, and N.A. Rayner (2013). EN4: Quality controlled ocean temperature and salinity profiles and monthly objective analyses with uncertainty estimates, *J. Geophys. Res. Oceans*, 118, 6704– 6716, DOI:[10.1002/2013JC009067](https://doi.org/10.1002/2013JC009067).

- Gharamti, M.E., J. Valstar, I. Hoteit (2014). An adaptive hybrid EnKF-OI scheme for efficient state-parameter estimation of reactive contaminant transport models. *Advances in Water Resources*, 72, 1-15, <http://dx.doi.org/10.1016/j.advwatres.2014.05.001>.
- Hamill, T. M., and C. Snyder (2000). A hybrid ensemble Kalman filter-3D variational analysis scheme. *Mon. Wea. Rev.*, 128 (8), 2905–2919.
- Hamill, T. M., J. S. Whitaker, and C. Snyder (2001). Distance-dependent filtering of background error covariance estimates in an ensemble Kalman filter. *Mon. Wea. Rev.*, 129, 2776–2790, DOI:10.1175/1520-0493(2000)128<2905:AHEKFV>2.0.CO;2.
- Hamill, T.M. (2006). Ensemble-based atmospheric data assimilation. *Predictability of Weather and Climate*, Palmer T.N., Hagedorn R. (eds). 124-156, Cambridge University Press, Cambridge, UK, accessible at <https://www.ecmwf.int/sites/default/files/elibrary/2003/9756-ensemble-based-data-assimilation.pdf> as on 1st June, 2020.
- Hoteit, I., D.T. Pham, and J. Blum (2002). A simplified reduced order Kalman filtering and application to altimetric data assimilation in Tropical Pacific. *Journal of Marine Systems*, 36, 101-127, DOI:10.1016/S0924-7963(02)00129-X.
- Hoteit, I., D. Pham, M.E. Gharamti, and X. Luo (2015). Mitigating Observation Perturbation Sampling Errors in the Stochastic EnKF. *Mon. Wea. Rev.*, 143, 2918–2936, DOI:10.1175/MWR-D-14-00088.1.
- Hoteit, I., et al., (2018). Data assimilation in oceanography: Current status and new directions. In "New Frontiers in Operational Oceanography", E. Chassignet, A.

Pascual, J. Tintoré, and J. Verron, Eds., *GODAE OceanView*, 465-512, DOI:10.17125/gov2018.ch17.

Hoteit, I., et al., (2020). Towards an End-to-End Analysis and prediction system for Weather, Climate, and Marine Applications in the Red Sea. *Bull. Ame. Met. Society*, Under Review.

Houtekamer, P. L., and H. L. Mitchell (1998). Data assimilation using an ensemble Kalman filter technique. *Mon. Wea. Rev.*, 126, 796–811, DOI:10.1175/1520-0493(1998)126<0796:DAUAEK>2.0.CO;2.

Holland, W.R. (1978). The Role of Mesoscale Eddies in the General Circulation of the Ocean—Numerical Experiments Using a Wind-Driven Quasi-Geostrophic Model. *J. Phys. Oceanogr.*, 8, 363–392, DOI:10.1175/15200485(1978)008<0363:TROMEI>2.0.CO;2.

Hunt, B.R., E.J. Kostelich, and I. Szunyogh (2007). Efficient data assimilation for spatiotemporal chaos: A local ensemble transform Kalman filter. *Physica D: Nonlinear Phenomena*, 230, 112-126, DOI: 10.1016/j.physd.2006.11.008.

Kalnay, E. (2002). Atmospheric Modeling, Data Assimilation and Predictability, *Cambridge University Press: Cambridge*, UK, DOI:10.1017/CB09780511802270.

Kamachi, M., Y. Fujii, and X. Zhou (2002). Ocean Data Assimilation in the Tropical Pacific: A Short Survey. *Journal of Oceanography*, 58, 45–55, DOI:10.1023/A:1015872600455

Konstantin, B., A. Kuleshov, N. Tuchkova, and C.A.S. Tanajura (2018). An optimal data assimilation method and its application to the numerical simulation of the ocean

dynamics. *Mathematical and Computer Modelling of Dynamical Systems*, 24:1, 12-25, DOI:10.1080/13873954.2017.1338300.

Krokos, G., V.P. Papadopoulos, S.S. Sofianos, H. Ombao, P. Dybczak, and I. Hoteit (2019). Natural climate oscillations may counteract Red Sea warming over the coming decades. *Geophysical Research Letters*, 46, 3454–3461, DOI: 10.1029/2018GL081397.

Large, W. G., J.C. McWilliams, and S.C. Doney (1994). Oceanic vertical mixing: a review and a model with a nonlocal boundary layer parameterization. *Reviews of Geophysics*, 32, 363–403, DOI:10.1029/94RG01872.

Large, W.G., G. Danabasoglu, S.C. Doney, and J.C. McWilliams (1997). Sensitivity to Surface Forcing and Boundary Layer Mixing in a Global Ocean Model: Annual-Mean Climatology. *J. Phys. Oceanogr.*, **27**, 2418–2447, DOI:10.1175/1520-0485(1997)027<2418:STSFAB>2.0.CO;2

Larsen, J., J.L. Hoyer, J. She (2007). Validation of a hybrid optimal interpolation and Kalman filter scheme for sea surface temperature assimilation. *Journal of Marine systems*, 65, 122-133, DOI: 10.1016/j.jmarsys.2005.09.013.

Leith, C.E. (1996). Stochastic models of chaotic systems. *Physica D: Nonlinear Phenomena*, 98, 2-4, 481-491, DOI: 10.1016/0167-2789(96)00107-8.

Lellouche, J.-M., O. Le Galloudec, M. Drévillon, C. Régnier, E. Greiner, G. Garric, N. Ferry, C. Desportes, C.E. Testut, C. Bricaud, R. Bourdallé-Badie, B. Tranchant, M. Benkiran, Y. Drillet, A. Daudin, and C. De Nicola (2013). Evaluation of global monitoring and forecasting systems at Mercator Océan, *Ocean Sci.*, 9, 57–81, DOI:10.5194/os-9-57-2013.

- Lorenc, A.C., N.E. Bowler, A.M. Clayton, and S.R. Pring (2015). Comparison of Hybrid-4DVar and Hybrid-4DVar data assimilation methods for Global NWP. *Monthly Weather Review*, 143, 212-229, DOI: 10.1175/MWR-D-14-00195.1.
- Luo, X. and I. Hoteit (2011). Robust Ensemble Filtering and Its Relation to Covariance Inflation in the Ensemble Kalman Filter. *Mon. Wea. Rev.*, 139, 3938-3953, DOI:10.1175/MWR-D-10-05068.1.
- Marshall, J., A. Adcroft, C. Hill, L. Perelman, and C. Heisey (1997). A finite-volume, incompressible Navier Stokes model for studies of the ocean on parallel computers. *J. Geophys. Res. Oceans*, 102 (C3) 5753–5766, <http://dx.doi.org/10.1029/96JC02775>.
- Mellor, G. L., and T. Yamada (1982). Development of a turbulence closure model for geophysical fluid problems, *Rev. Geophys.*, 20(4), 851–875, DOI:10.1029/RG020i004p00851.
- Mertz, F., V. Rosmorduc, C. Maheu, and Y. Faugere (2017). Product user manual, For sea level SLA products. *Technical Report CMEMS-SL-PUM-008-032-051*, issue 1.1.
- Moore, A.M., M.J. Martin, S. Akella, H.G. Arango, M. Balmaseda, L. Bertino, S. Ciavatta, B. Cornuelle, J. Cummings, S. Frolov, P. Lermusiaux, P. Oddo, P.R. Oke, A. Storto, A. Teruzzi, A. Vidard, and A.T. Weaver (2019). Synthesis of Ocean observations using data assimilation for operational, real-time and reanalysis systems: A more complete picture of the state of the ocean. *Front. Mar. Sci.*, 6:90, DOI:10.3389/fmars.2019.00090.
- Pacanowski, R.C., and S.G. Philander (1981). Parameterization of Vertical Mixing in Numerical Models of Tropical Oceans. *J. Phys. Oceanogr.*, **11**, 1443–1451, DOI:10.1175/1520-0485(1981)011<1443:POVMIN>2.0.CO;2.

- Parent, L., C.E. Testut, J.M. Brankart, J. Verron, P. Brasseur, and L. Gourdeau (2003). Comparative assimilation of Topex/Poseidon and ERS altimeter data and of TAO temperature data in the tropical Pacific ocean during 1994-1998, and the mean sea-surface height issue. *Jour. Marine Systems*, 40-41, 381-401, DOI:10.1016/S0924-7963(03)00025-5.
- Penny, S.G., D.W. Behringer, J.A. Carton, and E. Kalnay (2015). A Hybrid Global Ocean Data Assimilation System at NCEP. *Monthly Weather Review*, 143, 4660-4677, DOI:10.1175/MWR-D-14-00376.1.
- Pham D.T., J. Verron, and M.C. Roubaud (1998). A singular evolutive extended Kalman filter for data assimilation in oceanography. *Journal of Marine systems*, 16, 323-340, DOI: 10.1016/S0924-7963(97)00109-7.
- Quadfasel, D., and H. Baudner (1993). Gyre-scale circulation cells in the Red Sea. *Oceanol. Acta*, 16, 221-229, <https://archimer.ifremer.fr/doc/00099/21049/>.
- Raitsos, D.E., Y. Pradhan, R.J.W. Brewin, G. Stenchikov, and I. Hoteit (2013). Remote sensing the phytoplankton seasonal succession of the Red sea. *Plos one*, DOI:10.1371/journal.pone.0064909.
- Raitsos D.E., X. Yi, T. Platt, M.F. Racault, R.J.W. Brewin, Y. Pradhan, V.P. Papadopoulos, S. Sathyendranath, and I. Hoteit (2015). Monsoon oscillations regulate fertility of the Red Sea. *Geophysical Research Letters*, 42, 3, 855-862, DOI:10.1002/2014GL062882.
- Redi, M.H. (1982). Oceanic Isopycnal Mixing by Coordinate Rotation. *J. Phys. Oceanogr.*, 12, 1154–1158, DOI:10.1175/1520-0485(1982)012<1154: OIMBCR >2.0.CO;2

- Reynolds, R.W., T.M. Smith, C. Liu, D.B. Chelton, K.S. Casey, and M.G. Schlax (2007). Daily high-resolution blended analyses for sea surface temperature. *Journal of climate*, 20, 5473-5496 , DOI:10.1175/2007JCLI1824.1.
- Sanikommu, S. (2015). A study on global ocean analysis from an ocean data assimilation system and its sensitivity to observations and forcing fields, *Ph.D. thesis, Andhra University*. Available at http://www.incois.gov.in/documents/PhDThesis_Sivareddy.pdf.
- Sanikommu, S., A. Paul, T. Sluka, M. Ravichandran, and E. Kalnay (2017). The pre-Argo ocean reanalyses may be seriously affected by the spatial coverage of moored buoys. *Scientific Reports*, Vol. 7, 46685, DOI:10.1038/srep46685.
- Sanikommu, S., D.S. Benerjee, B. Baduru, B. Paul, A. Paul, K. Chakraborty, and I. Hoteit (2019). Impact of dynamical representational errors on an Indian Ocean ensemble data assimilation system. *Quart. Journ. Royal Met. Soc.*, DOI:10.1002/qj.3649.
- Sanikommu, S., H. Toye, P. Zhan, S. Langodhan, G. Krokos, O. Knio, and I. Hoteit (2020). Impact of atmospheric and model physics perturbations on a high-resolution ensemble data assimilation system of the Red Sea. *Journal of Geophysical Research-Oceans*, under review.
- Smagorinski, J. (1993). Large Eddy Simulation of Complex Engineering and Geophysical Flows. Edited by B. Galperin and S. A Orszag, *Cambridge University Press*. pp. 3-36, DOI:10.1017/S0022112095231768.
- Song, H., I. Hoteit, B.D. Cornuelle, A.C. Subramanian (2010). An adaptive approach to mitigate background covariance limitations in the ensemble Kalman filter. *Mon Weather Rev.*, 138, 2825–45. <http://dx.doi.org/10.1175/2010MWR2871.1>.

- Sofianos, S.S., and W.E. Johns (2002). An Oceanic General Circulation Model (OGCM) investigation of the Red Sea circulation: 1. Exchange between the Red Sea and the Indian Ocean. *J Geophys Res*, 107 (C11), 3196, DOI:10.1029/2001JC001184.
- Sofianos, S.S., and W.E. Johns (2003). An Oceanic General Circulation Model (OGCM) investigation of the Red Sea circulation: 2. Three dimensional circulation in the Red Sea. *J Geophys Res* 108 (C3), 3066, DOI:10.1029/2001JC001185.
- Stammer, D., M. Balmaseda, P. Heimbach, A. Köhl, and A. Weaver (2016). Ocean Data Assimilation in Support of Climate Applications: Status and Perspectives, *Annual Review of Marine Science*, 8,1, 491-518, DOI:10.1146/annurev-marine-122414-034113.
- Stark, J. D., C.J. Donlon, M.J Martin, and M.E. McCulloch (2007). OSTIA: An operational, high resolution, real time, global sea surface temperature analysis system. In *Oceans 2007-europe* pp. 14. Aberdeen, UK, DOI:10.1109/OCEANSE.2007. 4302251.
- Swinbank, R., M. Kyouda, P. Buchanan, L. Froude, T.M. Hamill, T.D. Hewson, J.H. Keller, M. Matsueda, J. Methven, F. Pappenberger, M. Scheuerer, H.A. Titley, L. Wilson, and M. Yamaguchi (2016). The TIGGE Project and Its Achievements. *Bull. Amer. Meteor. Soc.*, **97**, 49–67, DOI:10.1175/BAMS-D-13-00191.1
- Toye, H., P. Zhan, G. Gopalakrishnan, A.R. Kartadikaria, H. Huang, O. Knio, and I. Hoteit (2017). Ensemble data assimilation in the Red Sea: sensitivity to ensemble selection and atmospheric forcing. *Ocean Dynamics*. 67, 915–933, <http://dx.doi.org/10.1007/s10236-017-1064-1>.
- Tsiaras, K. P., I. Hoteit, S. Kalaroni, G. Petihakis, and G. Triantafyllou (2017). A hybrid ensemble-OI Kalman filter for efficient data assimilation into a 3-D biogeochemical

model of the Mediterranean. *Ocean Dynamics*, 67, 673–690, DOI:10.1007/s10236-017-1050-7.

Viswanadhapalli, Y., H.P. Dasari, S. Langodan, V.S. Challa, and I. Hoteit (2017). Climatic features of the Red Sea from a regional assimilative model. *Int. J. Climatol.*, 37: 2563-2581, DOI:10.1002/joc.4865.

Wan, L., Z. Jiang, W. Hui, Y. Changxiang, and L. Bertino (2009). A “Dressed” Ensemble Kalman filter using the Hybrid Coordinate ocean model in the Pacific. *Advances in Atmospheric Sciences*, 26, 5, 1042-1052, DOI:10.1007/s00376-009-7208-6.

Waters, J., M.J. Bell, M.J. Martin, and D.J. Lea (2017). Reducing ocean model imbalances in the equatorial region caused by data assimilation. *Quarterly Journal of Royal Meteorological society*, 143(702), 195-208, DOI:10.1002/qj.2912.

Xie, J., and J. Zhu (2010). Ensemble optimal interpolation schemes for assimilating Argo profiles into a hybrid coordinate ocean model. *Ocean Modelling*, 33(3), pp.283-298, DOI:10.1016/j.ocemod.2010.03.002.

Xuguang, W., T.M. Hamill, J.S. Whitaker, and C.H. Bishop (2007). A comparison of Hybrid Ensemble Transform Kalman filter-optimum interpolation and ensemble square root filter analysis schemes. *Mon. Weather Review*, 135, 1055- 1076, DOI:10.1175/MWR3307.1.

Yao, F.C., I. Hoteit, L.J. Pratt, A.S. Bower, A. Kohl, and G. Gopalakrishnan (2014a). Seasonal overturning circulation in the Red Sea: Part-1. Model validation and summer circulation. *J Geophys Res-Oceans*, 119, 2238–2262, DOI:10.1002/2013jc009004.

- Yao, F.C., I. Hoteit, L.J. Pratt, A.S. Bower, A. Kohl, G. Gopalakrishnan, and D. Rivas (2014b). Seasonal overturning circulation in the Red Sea: Part-2. Winter circulation. *J Geophys Res-Oceans*, 119,2263–2289, DOI:10. 1002/2013jc009331.
- Yao, F., and I. Hoteit (2018). Rapid red sea deep water renewals caused by volcanic eruptions and the North Atlantic Oscillation. *Science Advances*, **4**, 5637, DOI: 10.1126/sciadv.aar5637
- Zhai, P., A.S. Bower, W.M. Smethie-Jr., and L.J. Pratt (2015). Formation and spreading of Red Sea outflow water in the Red Sea. *Journal of Geophysical Research: Oceans*. 120, 6542-6563, DOI: 10.1002/2015JC010751.
- Zhan, P., G. Gopalakrishnan, A.C. Subramanian, D. Guo, and I. Hoteit (2018). Sensitivity studies of the Red sea eddies using adjoint method. *Journal of Geophysical Research-oceans*, 123(11), 8329-8345, DOI: 10.1029/2018JC014531.
- Zhan, P., G. Krokos, D. Guo, and I. Hoteit (2019). Three-dimensional signature of the Red Sea eddies and Eddy-induced transport: Signature of the red sea eddies and eddy-induced transport. *Geophysical Research Letters*, 46(4), DOI:10.1029/2018GL081387.
- Zuo, H., M.A. Balmaseda, S. Tietsche, K. Mogensen, and M. Mayer (2019). The ECMWF operational ensemble reanalysis–analysis system for ocean and sea ice: a description of the system and assessment, *Ocean Sci.*, 15, 779–808, DOI:10.5194/os-15-779-2019.

Tables with captions:

Table 1. Summary of the experiments conducted to demonstrate the skill of the Hybrid system in terms of improved ocean state. In the table “Random” model physics refers to the use of a time-varying ensemble of physics during the model integration of each ensemble member for forecasting.

Experiment	Initial condition	Atm. Forcing	Model physics	Assimilated observations	Assimilation Category
<i>Exp</i>	Single member on 1 st January, 2011	Ensemble mean	Standard	None	NA
<i>EnOIexpSCLexp</i>	Single member on 1 st January, 2011	Ensemble mean	Standard	Reynolds-SST, Altimeter SSH, and in situ temperature and salinity	EnOI before scaling quasi-static-seasonal ensemble of size 300
<i>EnOIexp</i>	Single member on 1 st January, 2011	Ensemble mean	Standard	Reynolds-SST, Altimeter SSH, and in situ temperature and salinity	EnOI with scaled quasi-static-seasonal ensemble of size 300
<i>EAKFexp</i>	50-member ensemble on 1 st January, 2011	50-member ensemble	Random	Reynolds-SST, Altimeter SSH, and in situ temperature and salinity	50 member EAKF

<i>HyBDexp</i>	50-member ensemble on 1 st January, 2011	50-member ensemble	Random	Reynolds-SST, Altimeter SSH, and in situ temperature and salinity	Hybrid with quasi-static-seasonal ensemble of size 250 and dynamic ensemble of size 50
<i>HyBDmPexp</i>	Same as <i>HyBDexp</i>	Same as <i>HyBDexp</i>	Standard	Same as <i>HyBDexp</i>	Same as <i>HyBDexp</i>
<i>HyBDmAPexp</i>	Same as <i>HyBDexp</i>	Ensemble mean	Standard	Same as <i>HyBDexp</i>	Same as <i>HyBDexp</i>

Table 2. Summary of EAKF and Hybrid assimilation experiments conducted to examine the computational efficiency of the hybrid system.

Experiment	Initial condition	Atm. Forcing	Assimilation Category
<i>EAKF100exp</i>	100-member ensemble on 1 st January, 2011	100-member ensemble	100-member EAKF
<i>EAKF250exp</i>	250-member ensemble on 1 st January, 2011	250-member ensemble	250-member EAKF
<i>EAKF500exp</i>	500-member ensemble on 1 st January, 2011	500-member ensemble	500-member EAKF
<i>HyBD30exp</i>	30-member ensemble on 1 st January, 2011	30-member ensemble	Hybrid with quasi-static-seasonal ensemble of size 270 and dynamic ensemble of size 30
<i>HyBD20exp</i>	20-member ensemble on 1 st January, 2011	20-member ensemble	Hybrid with quasi-static-seasonal ensemble of size 280 and dynamic ensemble of size 20

<i>HyBD10exp</i>	10-member ensemble on 1 st January, 2011	10-member ensemble	Hybrid with quasi-static-seasonal ensemble of size 290 and dynamic ensemble of size 10
------------------	---	--------------------	--

Table 3. Dictionary of model physics and associated coefficients considered in the experiments that use perturbed physics. Coefficients of vertical mixing schemes vary according to the standard values in MITgcm, unless otherwise stated. In the table, entries in first row indicate the standard scheme.

Horizontal Viscosity	Vertical Mixing	Horizontal diffusion
Simple-Harmonic with viscosity coefficient $30 \text{ m}^2/\text{s}$	KPP- <i>Large et al.</i> (1994)	Implicit diffusion for temperature and salinity
Simple-Bi-harmonic scheme of <i>Holland</i> (1978) with viscosity coefficient $10^7 \text{ m}^4/\text{s}$	PP81- <i>Pacanowski and Philander</i> (1981)	Explicit coefficients of $100 \text{ m}^2/\text{s}$ for temperature and salinity
Harmonic flavor of combined <i>Smagorinsky</i> (1993) and <i>Leith</i> (1996) schemes with viscosity coefficient $30 \text{ m}^2/\text{s}$, Smag coefficient 2.5 and Leith coefficient 1.85	MY82- <i>Mellor and Yamada</i> (1982)	Gent-McWilliams/Redi (<i>Redi</i> , 1982; <i>Gent and McWilliams</i> , 1990; <i>Gent et al.</i> , 1995) using slope clipping of <i>Cox</i> (1987), with background diffusion set to $100 \text{ m}^2/\text{s}$
	GGL90- <i>Gaspar et al.</i> (1990)	Gent-McWilliams/Redi (<i>Redi</i> , 1982; <i>Gent and McWilliams</i> , 1990; <i>Gent et al.</i> , 1995) using tapering scheme of <i>Danabasoglu and McWilliams</i> , (1995) with background diffusion set to $100 \text{ m}^2/\text{s}$
		Gent-McWilliams/Redi (<i>Redi</i> , 1982; <i>Gent and McWilliams</i> , 1990; <i>Gent et al.</i> , 1995) using tapering scheme of

		<i>Large et al.</i> , (1997) with background diffusion set to 100 m ² /s
--	--	---

Table 4. Statistics of computational expenditure, in terms of core-hours, associated with different assimilation experiments. In the table, we show computational expenditure incurred for each component of the assimilation system: the ocean model MITgcm, the first part of assimilation code DART, and the second part of assimilation code, HDART. Note that the HyBDexp systems run two assimilation codes, DART and HDART, parallelly.

Experiment	MITgcm	DART	HDART	Total	improvement (%)
<i>EAKF250exp</i>	1140	40	NA	1180	NA
<i>HyBDexp</i>	228	7	40	275	76
<i>HyBD10exp</i>	46	3	40	89	92

Figures with captions:

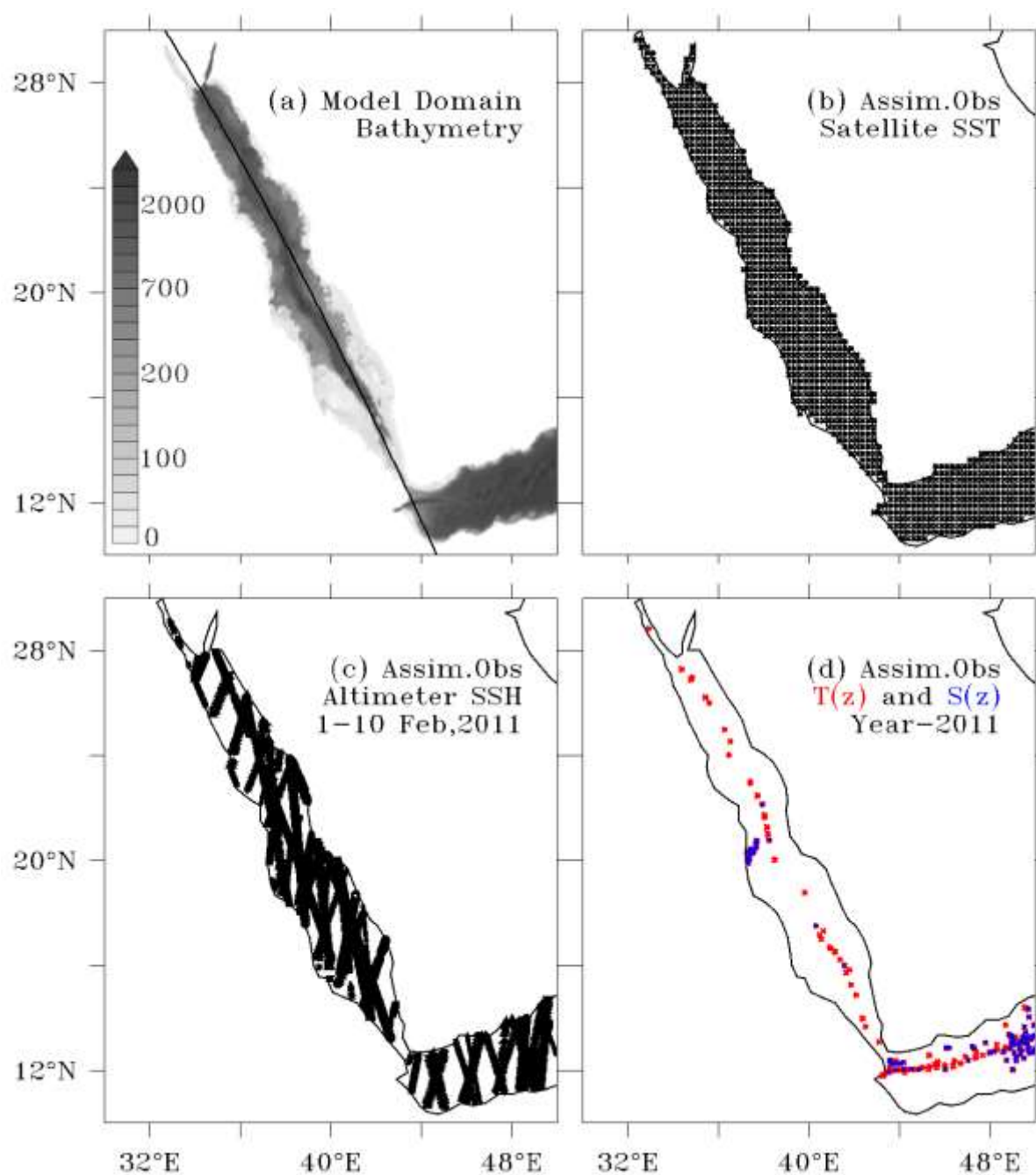


Figure 1. (a) Model domain and bathymetry (m). Thick black line represents the Red Sea axis. Panels (b-d) respectively indicate the geographical coverage of assimilated observations of satellite based level-4 sea surface temperature-SST observations on a typical day, satellite level-3 sea surface height-SSH measurements over a typical altimeter period, and EN4.2.1 in situ temperature (red) and salinity (blue) profiles available over the entire year 2011.

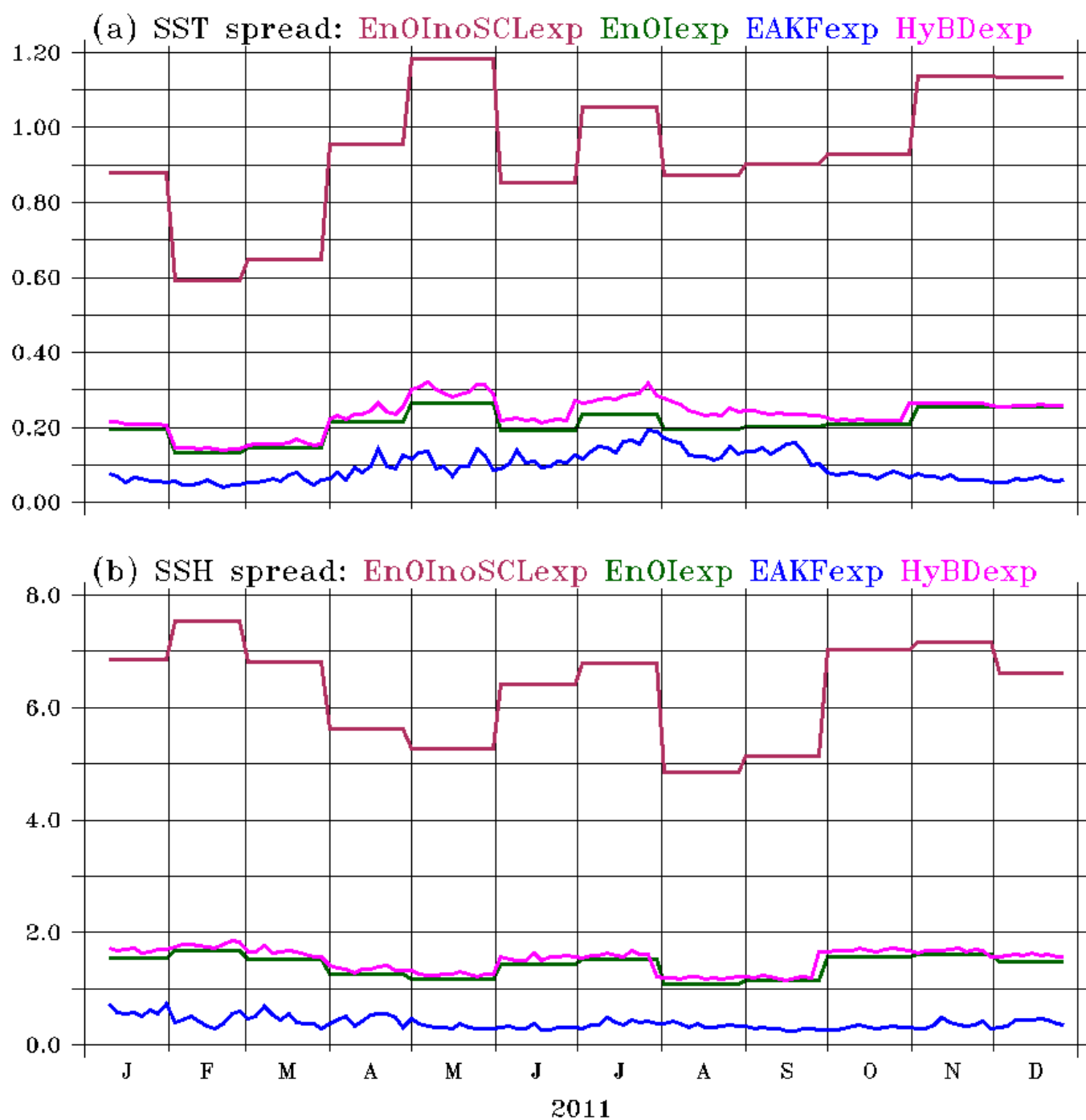


Figure 2. Domain averaged ensemble spread of (a) SST and (b) sea surface height SSH from *EnOInoSCLexp* (green-dash), *EnOlexp* (green-line), *EAKFexp* (blue-line) and *HyBDexp* (pink-line). Units of SST and SSH spread are in °C and cm.

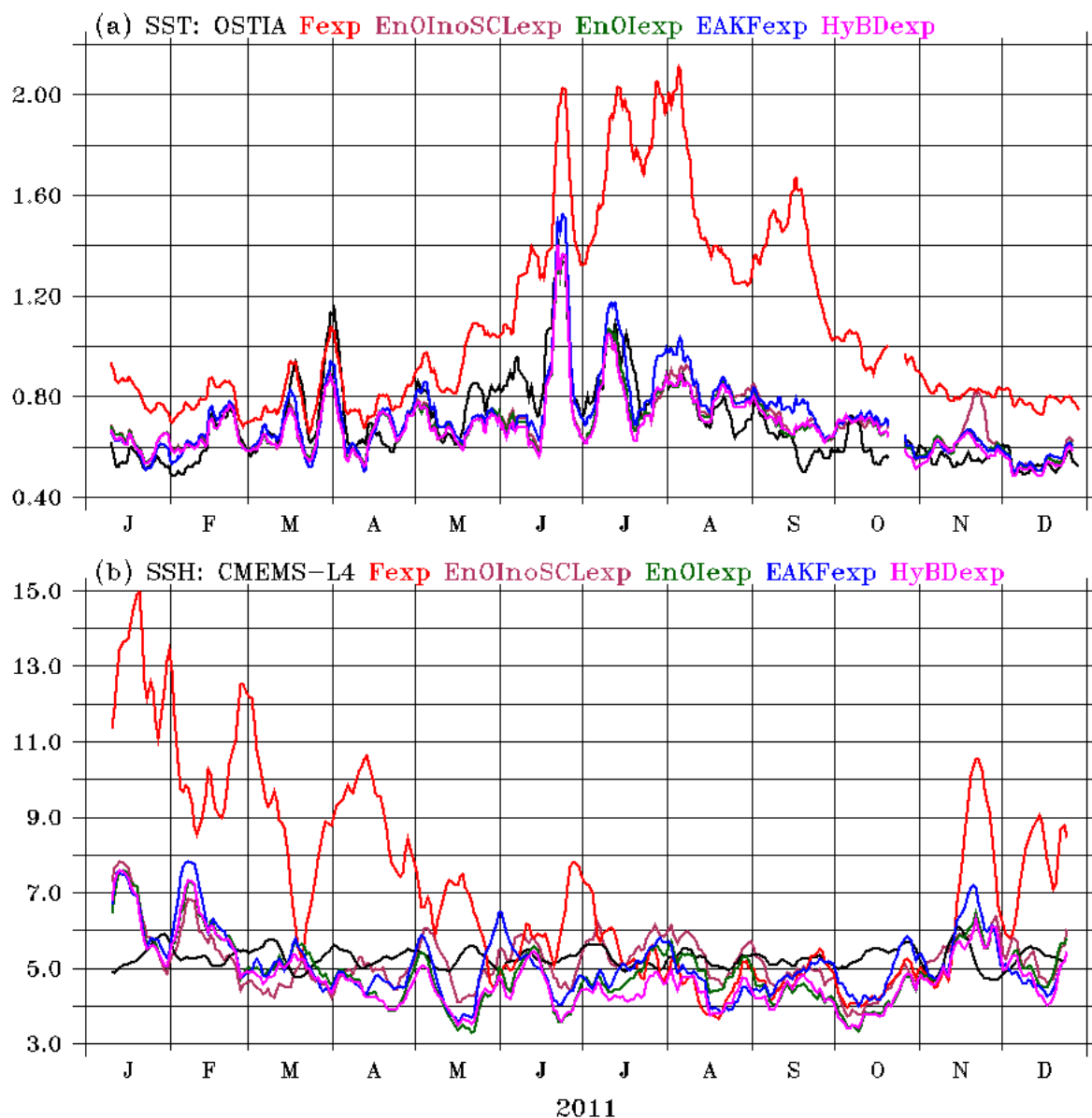


Figure 3. Time series of Root-Mean-Square-Difference (RMSD) for daily averaged (a) SST ($^{\circ}\text{C}$) and (b) SSH (cm) from level-4 gridded products (OSTIA for SST and CMEMS-L4 for SSH; black), *Fexp* (red), *EnOIInoSCLe xp* (magenta), *EnOIexp* (green), *EAKFexp* (blue), and *HyBDexp* (pink). SST RMSD (SSH RMSD) is computed by collocating the daily averaged model forecasts in the whole model domain onto level-3 GHRSSST (level-3 altimeter observations) product. 10-day smoothing is applied to better highlight the differences between the assimilation results.

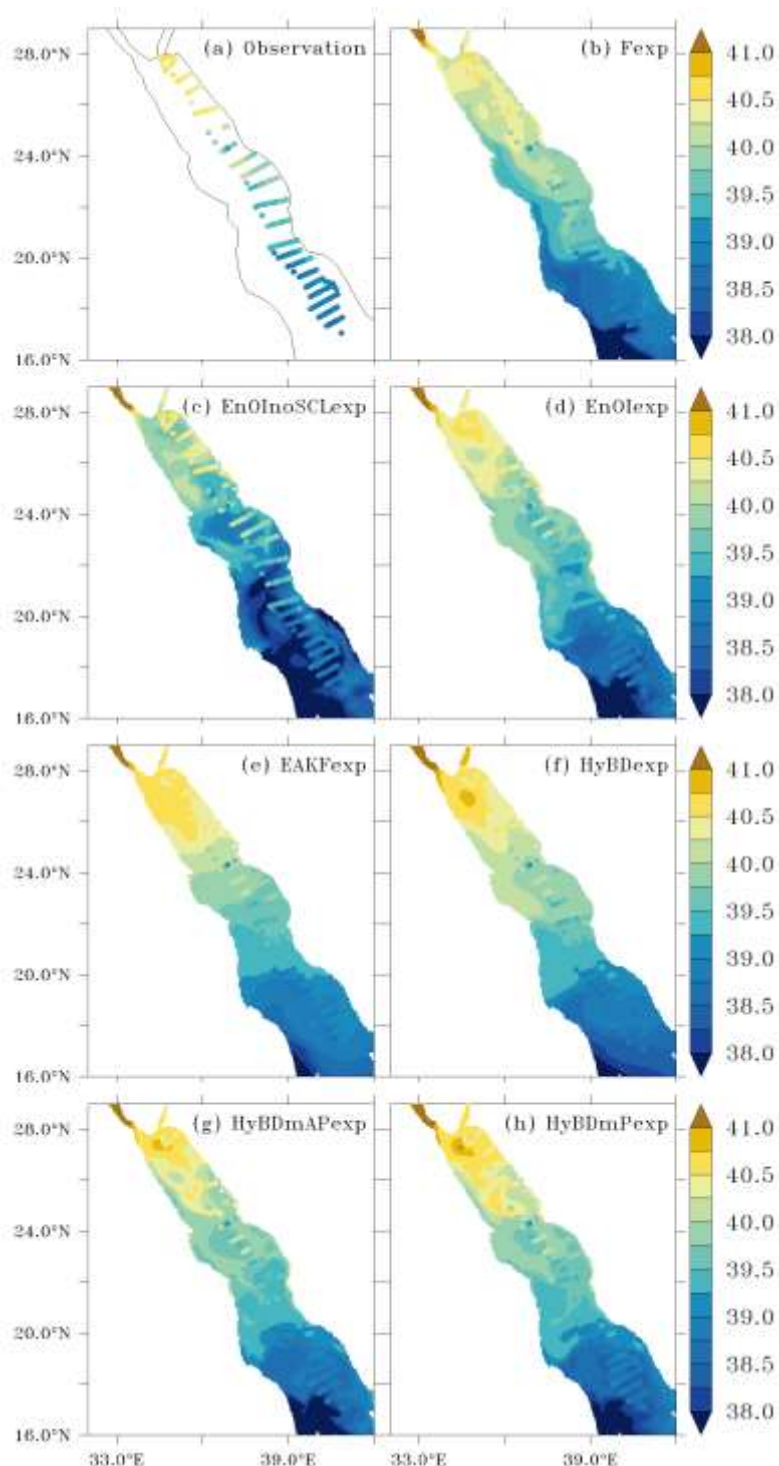


Figure 4. SSS (psu) from (a) WHOI/KAUST summer cruise, (b) Fexp, (c) *EnOIInoSCExp*, (d) *EnOIexp*, (e) *EAKFexp*, (f) *HyBDexp*, (g) *HyBDmAPexp*, and (h) *HyBDmPexp*. The SSS from the model experiments is the time average between 15th September -8th October, 2011, pertaining to the WHOI/KAUST summer cruise. SSS of WHOI/KAUST is overlaid on the spatial maps also for model-data comparison.

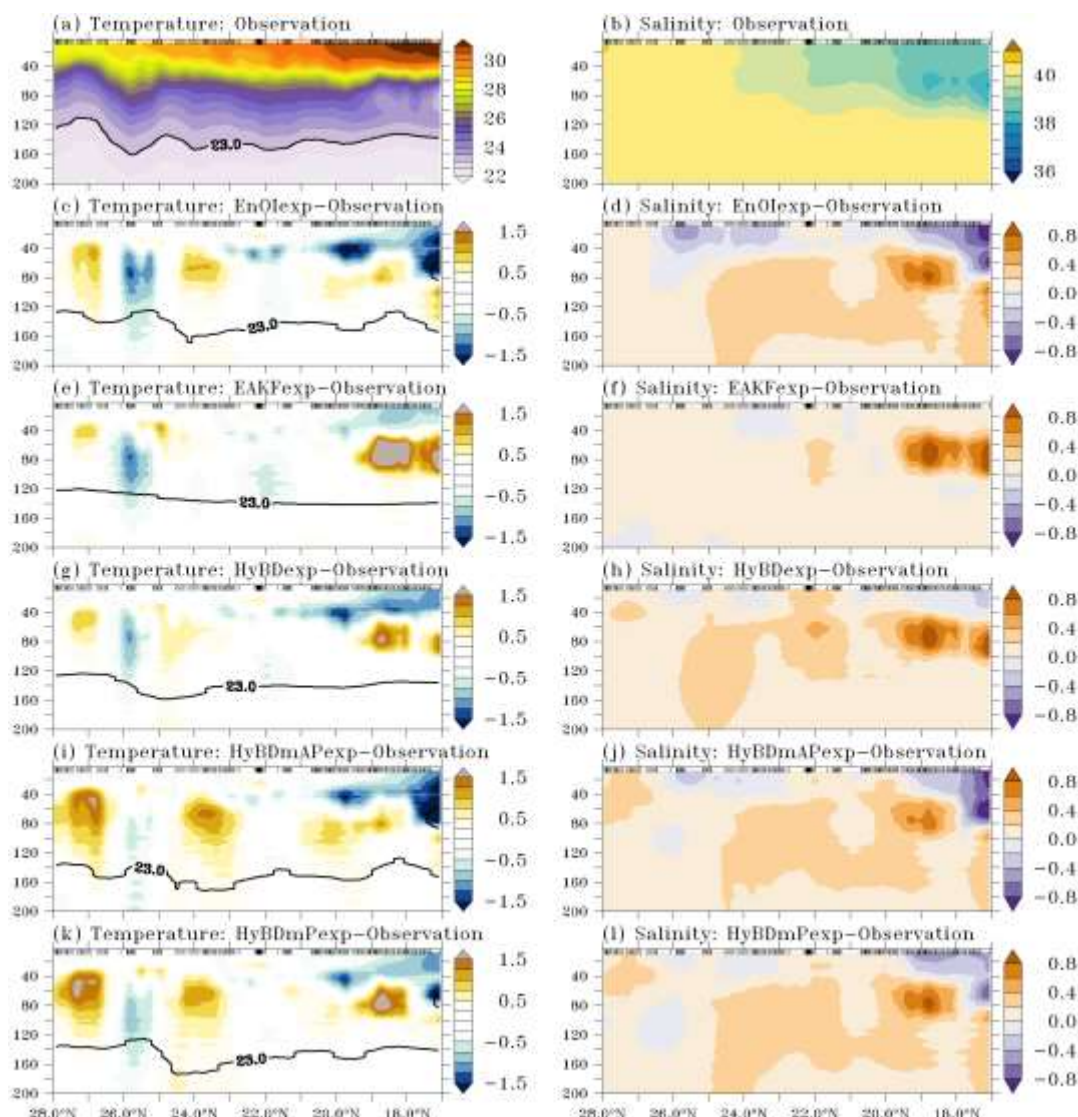


Figure 5. Subsurface temperature (°C) and salinity (psu) from *in-situ* CTD observations (a-b) collected during the WHOI/KAUST summer cruise conducted during 15th September – 8th October, 2011. Panels b(c), d(e), f(g), h(i), and j(k) show collocated (in space and time) temperature (salinity) differences between *EnOIexp* and WHOI/KAUST observations, *EAKFexp* and WHOI/KAUST observations, *HyBDexp* and WHOI/KAUST observations, *HyBDmAPexp* and WHOI/KAUST observations, and *HyBmPDexp* and WHOI/KAUST observations respectively. Temperature and salinity observations are smoothed by 1° and 10m in latitudinal and vertical directions to better highlight subsurface features. 23°C isotherm is also indicated in the respective temperature plots. Latitudes corresponding to observations locations are indicated as black vertical dashes at the top of each panel.

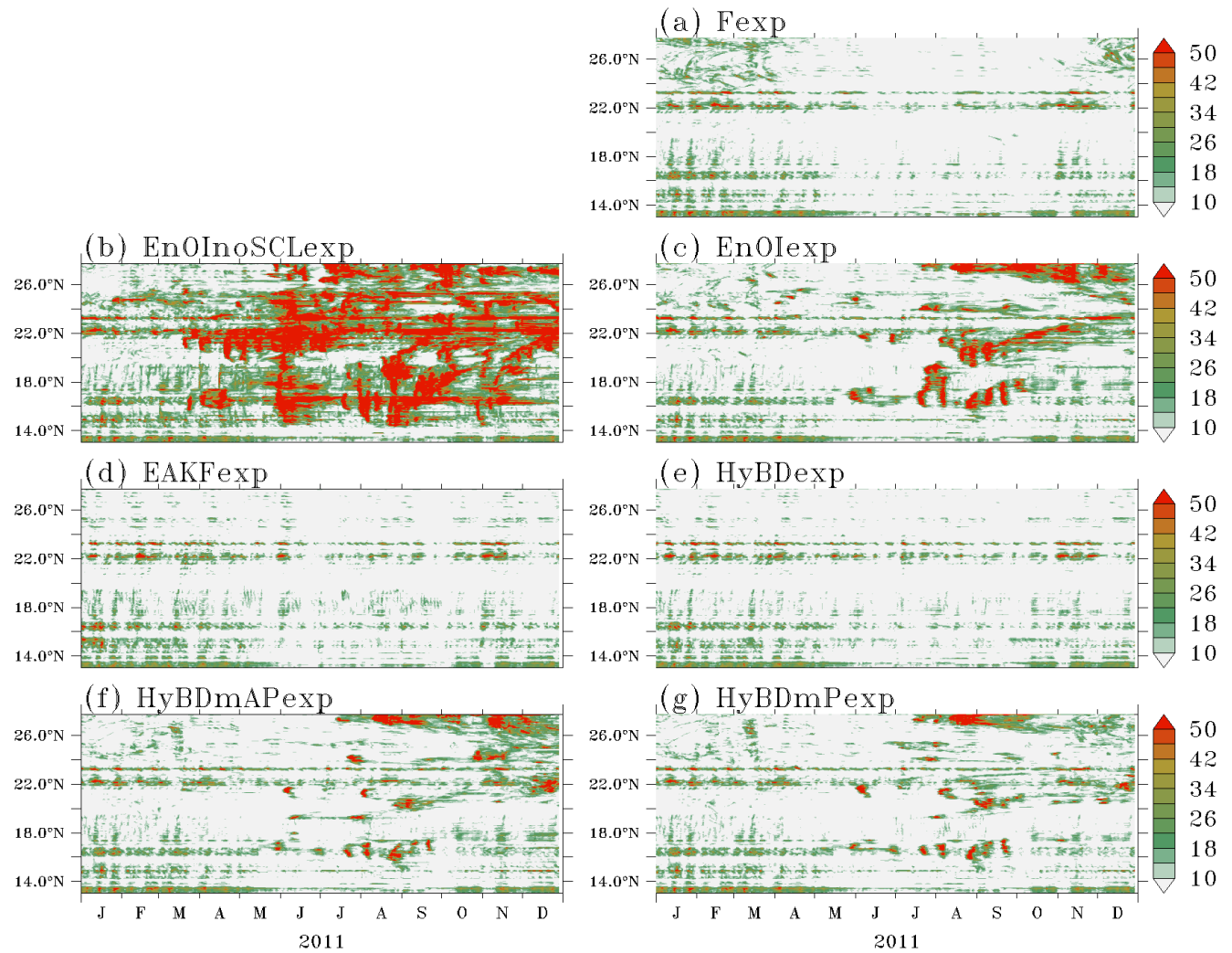


Figure 6. Temporal evolution of $|W(z)|_{max}$ (m/day) from the daily averaged vertical velocity in the ocean column along the axis of the Red sea (indicated in Figure 1a) from (a) *Fexp*, (b) *EnOI_{no}SCLe_{exp}*, (c) *EnOI_{exp}*, (d) *EAKF_{exp}*, (e) *HyBD_{exp}*, (f) *HyBD_mAP_{exp}*, and (g) *HyBD_mP_{exp}*.

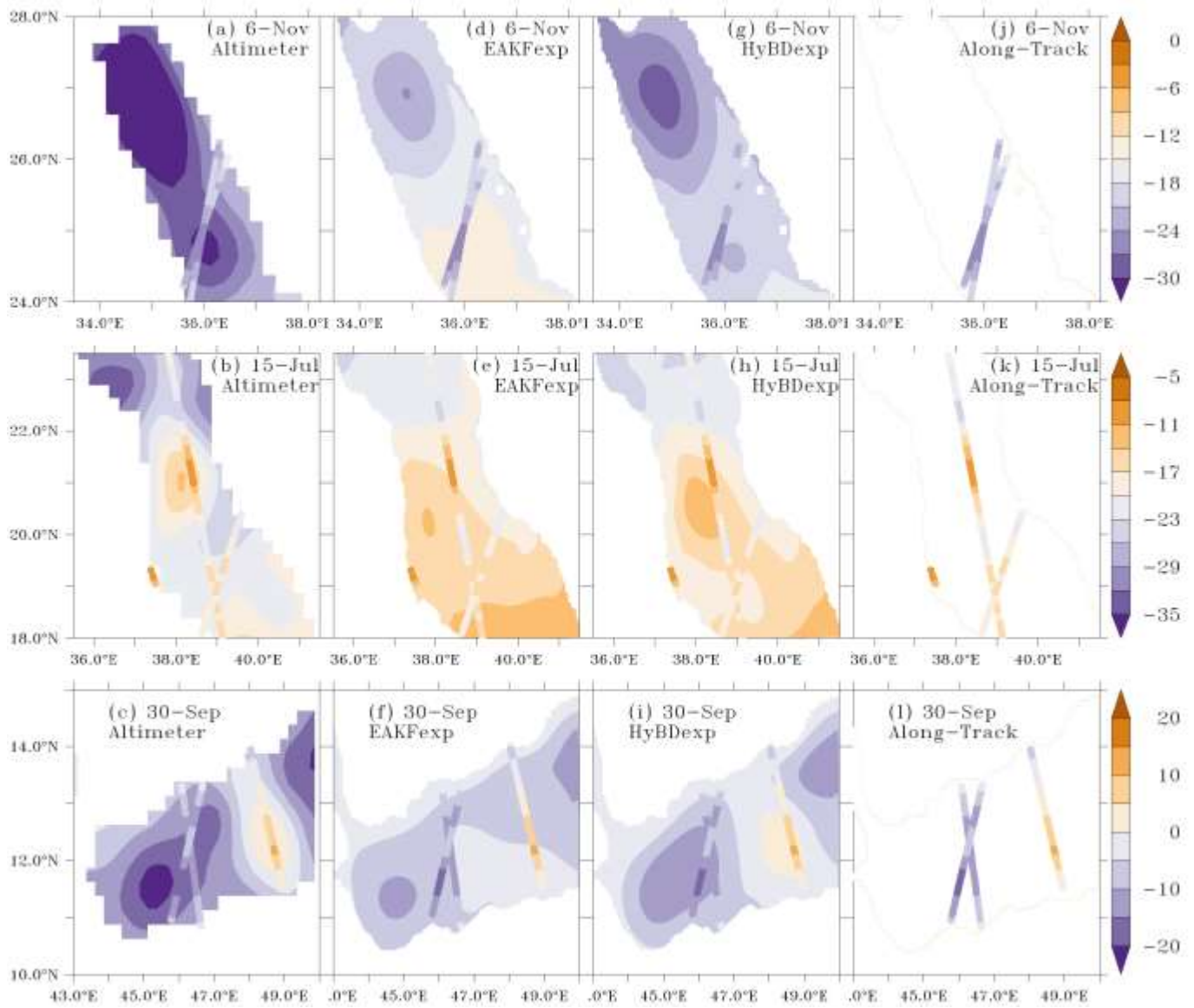


Figure 7. Spatial maps of daily averaged SSH (in cm) corresponding to 6th November, 2011 (top), 15th July, 2011 (middle), and 30th September, 2011 (bottom) from (a-c) merged altimeter CMEMS-L4. Panels (d-f), (g-i), and (j-l) show similar plots as resulted from *EAKFexp* and *HyBDexp* forecasts, and along-track observations, respectively. Along track SSH observations of the corresponding day is also overlaid on each map.

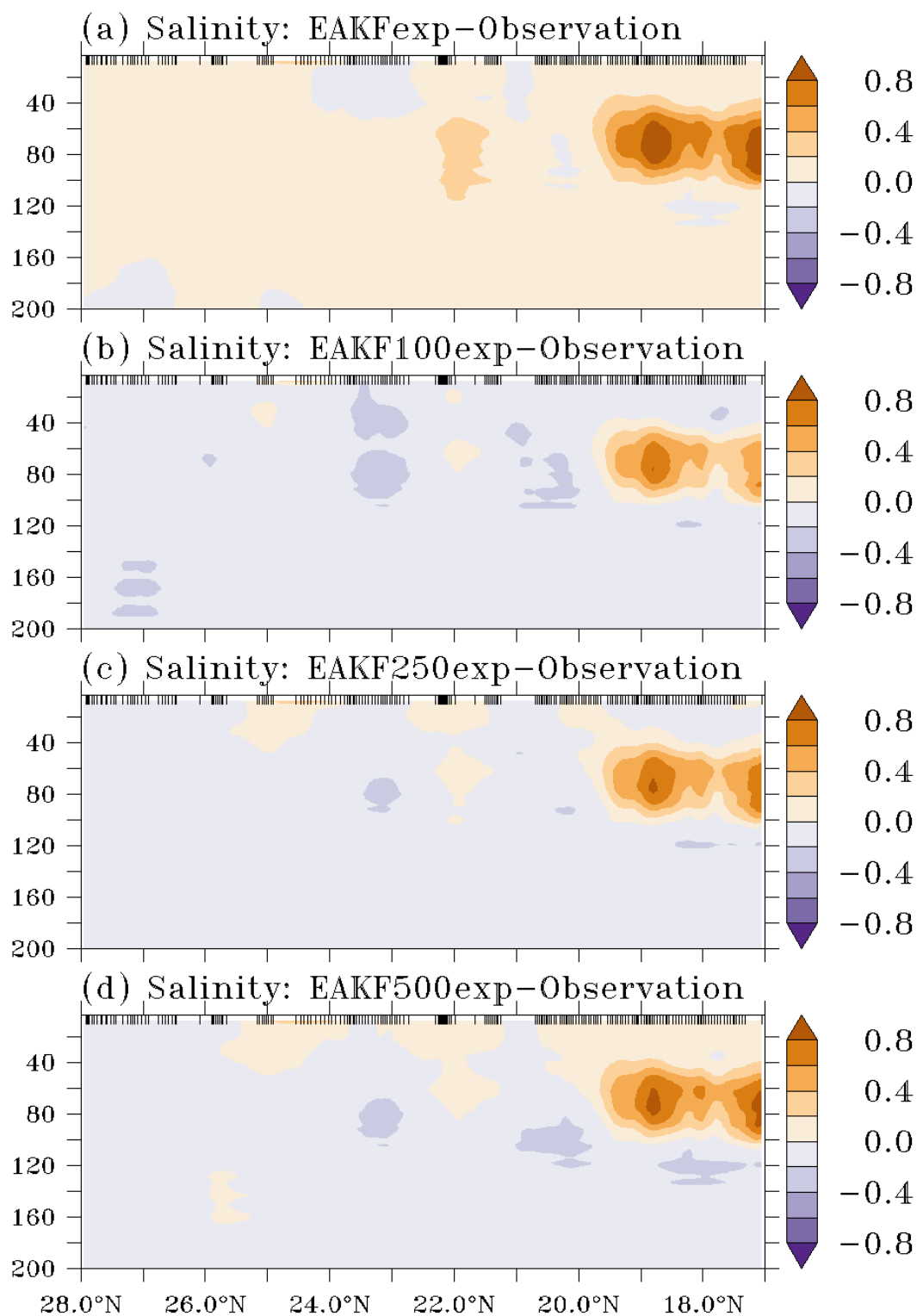


Figure 8. Collocated salinity differences (psu) between (a) *EAKFexp* simulations and WHOI/KAUST observations, (b) *EAKF100exp* simulations and WHOI/KAUST observations, (c) *EAKF250exp* simulations and WHOI/KAUST observations, and (d) *EAKF500exp* simulations and WHOI/KAUST observations.

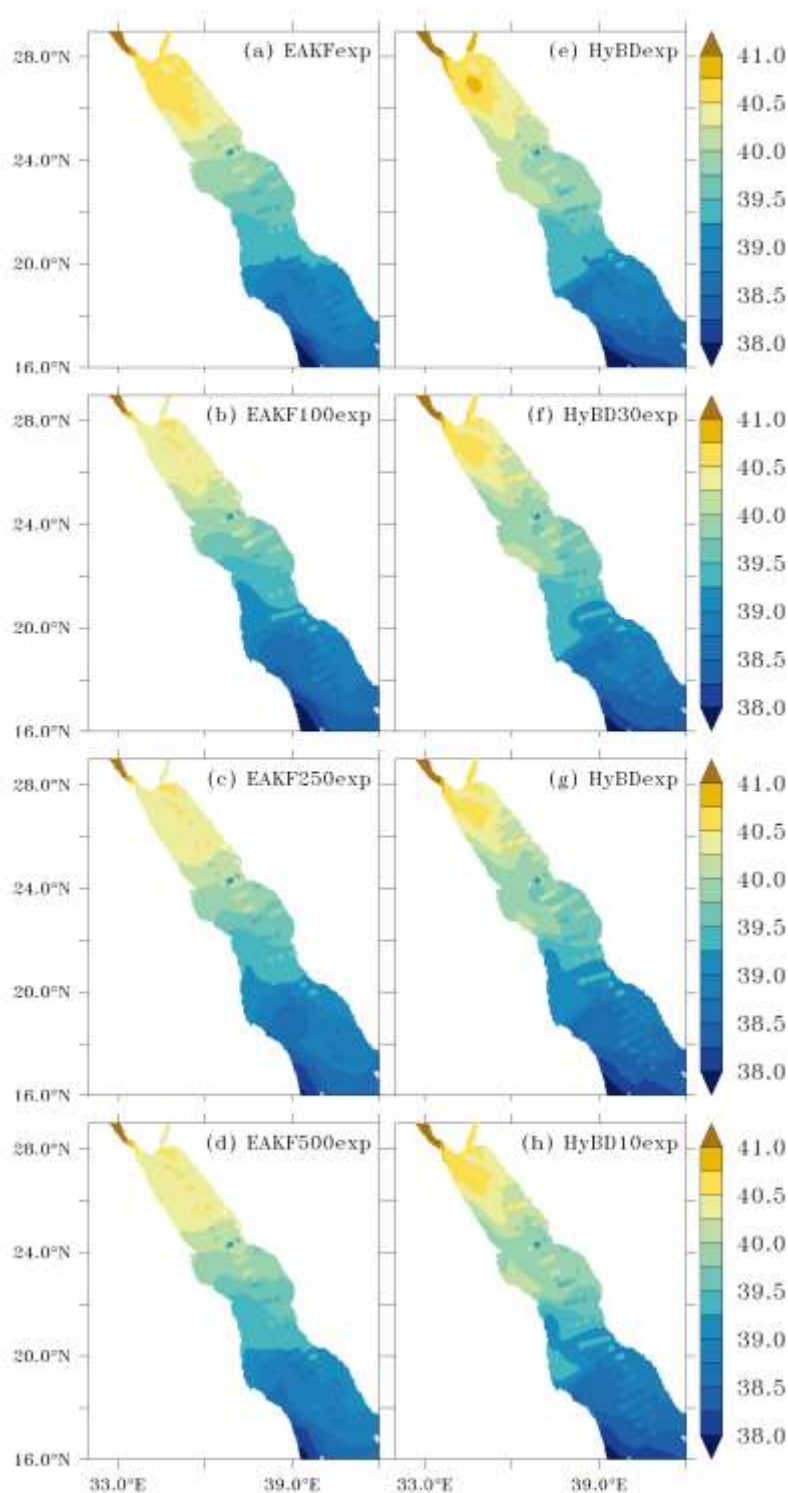


Figure 9. Same as Figure 4 except that the results are shown for various EAKF (top) and Hybrid (bottom) sensitivity experiments pertained to the size of the ensemble. Panels a-d corresponds to *EAKFexp*, *EAKF100exp*, *EAKF250exp*, and *EAKF500exp*, respectively. Similarly, e-h corresponds to *HyBDexp*, *HyBD30exp*, *HyBD20exp*, and *HyBD10exp*, respectively.